INL/RPT-24-76937 Rev0

Sodium-Cooled Fast Reactor Reference Plant Model

March 2024

Stefano Terlizzi[1], Namjae Choi[1], Jackson Harter[1], Ishita Trivedi[1], Travis Mui[2], and Javier Ortensi[1]

[1]*Reactor Physics Methods and Analysis, Idaho National Laboratory*
[2]*Nuclear Science and Engineering Division, Argonne National Laboratory*

INL is a U.S. Department of Energy National Laboratory
operated by Batelle Energy Alliance, LLC

DISCLAIMER

This information was prepared as an account of work sponsored by an agency of the U.S. Government. Neither the U.S. Government nor any agency thereof, nor any of their employees, makes any warranty, expressed or implied, or assumes any legal liability or responsibility for the accuracy, completeness, or usefulness, of any information, apparatus, product, or process disclosed, or represents that its use would not infringe privately owned rights. References herein to any specific commercial product, process, or service by trade name, trademark, manufacturer, or otherwise, does not necessarily constitute or imply its endorsement, recommendation, or favoring by the U.S. Government or any agency thereof. The views and opinions of authors expressed herein do not necessarily state or reflect those of the U.S. Nuclear Regulatory Commission.

INL/RPT-24-76937 Rev0

Sodium-Cooled Fast Reactor Reference Plant Model

Stefano Terlizzi[1], Namjae Choi[1], Jackson Harter[1], Ishita Trivedi[1], Travis Mui[2], and Javier Ortensi[1]

[1]**Reactor Physics Methods and Analysis, Idaho National Laboratory**
[2]**Nuclear Science and Engineering Division, Argonne National Laboratory**

March 2024

Idaho National Laboratory
Nuclear Science and Technology
Idaho Falls, Idaho 83415

http://www.inl.gov

Prepared for the
Office of Nuclear Regulatory Research
U. S. Nuclear Regulatory Commission
Washington, D. C. 20555
Task Order No.: 31310019F0015

Page intentionally left blank

SUMMARY

This report details the progress of Idaho National Laboratory (INL) in creating a reference plant multiphysics model for the Advanced Burner Test Reactor (ABTR). This model was developed under Task 13 of the U.S. Nuclear Regulatory Commission project "Development and Modeling Support for Advanced Non-Light Water Reactors," and is an extension of the reference plant model developed in Task 4b, which was improved upon in the following ways. (1) The discrete ordinates method was used in lieu of the super-homogenization (SPH)-corrected diffusion approximation in order to better capture the anisotropic scattering contribution and the neutron leakage change due to thermal expansion. (2) The novel neutronic spatial discretization approach, termed the ring-heterogeneous (RH) approximation, was conceptualized and introduced to capture the differential expansion of the materials in the core. This new technique proved capable of preserving fission rates and maintaining the eigenvalue within 2.5% and 266 pcm with 9 neutron energy groups, respectively. Separating the different materials in the core enables the differential expansion of materials to be explicitly accounted for, eliminating the need for problem-specific cross-section functionalization techniques. (3) The SAM model for the core and system thermal-hydraulics analysis was updated to include 61 channels instead of just four representative ones. This enables users to obtain improved spatial resolution for sodium temperature and density scalar fields. (4) All the mesh files were created via the Multiphysics Object-Oriented Simulation Environment (MOOSE) Reactor module, eliminating all reliance on external tools for mesh creation. (5) Finally, the fuel axial expansion now leverages the HT9 and UPuZr material properties that have been validated against experimental data. The reference plant model was used to perform a full-core unprotected loss of flow (ULOF) transient calculation, including neutronics, thermal and mechanical feedback mechanisms. Future work will be devoted to further enhancements of the model. Potential improvements to the model include the addition of the control rod driveline expansion feedback and the upgrading of the support plate model so as to explicitly include 3D effects. Additionally, a Nuclear Energy Advanced Modeling and Simulation funded parallel effort has completely automated the creation of the ring-heterogeneous (RH) mesh from the fully heterogeneous (FH) geometry, thus maximizing user friendliness for the sodium fast reactor sodium-cooled fast reactor (SFR) workflow and will be incorporated in future work.

ACKNOWLEDGEMENTS

The authors would like to acknowledge the contribution of Guillaume Giudicelli and Yaqi Wang for their assistance with troubleshooting issues in the MultiApps systems and Griffin, respectively. We also thank our former INL colleague Cole Mueller for developing the System Analysis Module (SAM) model with 61 channels and Rui Hu at ANL for helping develop the latest SAM model. Additionally, we wish to thank Yaqi Wang for his contributions to the conceptualization of the ring-heterogeneous (RH) and to Hansol Park for his suggestions regarding the final version of the RH approach, with improved topology between the clad and the fuel (i.e. fuel sandwiched between layers of clad). Finally, we want to thank Tarek Zaki, Andrew Bielen, and Jason Thompson of the Nuclear Regulatory Commission (NRC) for their valuable feedback and comments.

Specific contributions from the various authors:

1. Stefano Terlizzi - Conceptualization, Development of multiphysics and thermomechanical models; Formal analysis, Investigation, Writing, Review & editing, Visualization, Supervision.

2. Namjae Choi - Neutronics model development and verification, Formal analysis, Writing, Visualization.

3. Jackson Harter - Development of multiphysics and thermomechanical models.

4. Ishita Trivedi - Support for the development of MC^2-3 assembly models for cross sections generation.

5. Travis Mui - Support for the development of the thermal hydraulic models.

6. Javier Ortensi - Conceptualization, Development of MC^2-3 cross sections, Development of multiphysics and neutronics models; Supervision, Project administration.

This research made use of the resources provided by the Nuclear Energy Advanced Modeling and Simulation (NEAMS) program managed by the Department of Energy's Office of Nuclear Energy, and of the resources of the High Performance Computing Center at Idaho National Laboratory, which is supported by the Office of Nuclear Energy of the U.S. Department of Energy and the Nuclear Science User Facilities under contract no. DE-AC07-05ID14517.

Page intentionally left blank

CONTENTS

FIGURES

TABLES

ACRONYMS

ABTR	Advanced Burner Test Reactor
ANL	Argonne National Laboratory
CMFD	coarse mesh finite difference
CRAB	Comprehensive Reactor Analysis Bundle
FH	fully heterogeneous
INL	Idaho National Laboratory
MOOSE	Multiphysics Object-Oriented Simulation Environment
NEAMS	nuclear energy advanced modeling and simulation
RH	ring-heterogeneous
SAM	System Analysis Module
SFR	sodium-cooled fast reactor
SPH	super-homogenization
SRH	simplified ring-heterogeneous
ULOF	unprotected loss of flow

Page intentionally left blank

1. INTRODUCTION

This report details the progress and activities of Idaho National Laboratory (INL) in regard to the U.S. Nuclear Regulatory Commission project entitled "Development and Modeling Support for Advanced Non-Light Water Reactors."

Table 1 summarizes the tasks completed between 10/1/2022 and 11/30/2023 (i.e., the tasks documented in this report). It lists the deliverable numbers and statement-of-work tasks, and offers a brief description of the deliverables.

Table 1: List of deliverables.

Deliverable Number	SOW Task	Description
13	13	Development of a reference plant model for the Advanced Burner Test Reactor, using BlueCRAB. (This is an extension of the model developed under Task 4b.)
18	18	Documentation of the work performed under Task 13 partly fulfills deliverable 18.

The previously completed tasks documented in this report are: **Task 13**. Reference plant model for an sodium-cooled fast reactor (SFR):

1. Extension of the model produced under Task 4b to a reference plant model for a SFR
2. Support for analyses of unprotected loss of flow (ULOF) transients.
3. Support for the development of microscopic/macroscopic cross sections for SFR designs.

2. BACKGROUND AND PROBLEM DESCRIPTION

To establish a reference plant model for an SFR, the Advanced Burner Test Reactor (ABTR) benchmark specifications reported in Ref. [6] were used. This design was chosen because it is generic enough to avoid any proprietary concerns, yet specific enough to capture the primary design characteristics of the envisioned sodium fast reactors. To date, the ABTR computational model here presented is the most advanced nuclear energy advanced modeling and simulation (NEAMS) model including thermomechanical feedback mechanisms. In this work, microscopic cross-section libraries were generated using the Griffin/MC^2-3 platform, adopting the ANL-9 group structure. These cross sections are leveraged within a novel spatial homogenization strategy, labeled simplified ring-heterogeneous (SRH) [7]. This SRH spatial homogenization strategy represents the rings of fuel pins within each assembly as solid hexagonal rings separated by coolant rings. The adopted SRH model allows for the capture of differential expansion among various materials while avoiding the complexity of the fully-heterogeneous mesh. The Griffin discontinuous finite element, discrete ordinates solver, accelerated through the coarse mesh finite difference (CMFD) method, is used to provide coupled transient simulations with thermomechanics and heat transfer. The coupling of the neutronics with the themomechanical and the fluid heat transfer models allows to capture the following feedback mechanisms during the ULOF transient scenario [8]:

- **Radial expansion feedback**. This is the strongest feedback among the ones affecting SFR dynamic response during the ULOF accident scenario. The feedback mechanism arises from the radial expansion of the hex-can load pads and the support grid plate on top of which the fuel assemblies are situated. The plate's expansion increases the core pitch, together with the surface area available for neutrons to leak outside the core. The increase in neutron leakage due to the radial expansion decreases the core reactivity, thus ensuring the reactor's self-regulation.

- **Fuel Doppler feedback**. This feedback is caused by an increase in parasitic neutron capture in the fuel due to the resonance Doppler broadening, primarily from U-238. The fuel Doppler feedback mechanism is a positive reactivity contribution during most of the ULOF accident

scenario due to the decrease in fuel temperature.

- **Axial fuel expansion feedback**. This feedback is caused by two phenomena: (1) thermal expansion, and (2) irradiation-induced swelling driven by the growth of fission product gas bubbles as the fuel is irradiated. We include the thermal expansion of the fuel in the axial direction in this work and the consequential increase in lateral surface area. This leads to an increase in neutron leakage, thereby reducing reactivity. As noticed for the fuel Doppler feedback, within the ULOF accident scenario, this is a positive reactivity contribution due to the decrease in fuel temperature and the fuel axial contraction.

- **Sodium density and temperature feedback**. This neutronics feedback results from the superposition of three phenomena consequent to the sodium density decrease: (1) Reduction of neutron moderation and a hardening of the neutron spectrum, leading to lower Pu239 capture (2) Reduced sodium capture, and (3) increased neutron leakage. The feedback is globally positive, but it is characterized by a lower magnitude with respect to the ones listed above [9].

2.1 Assumptions and Simplifications

This section lists the main assumptions and simplifications of the current model. A detailed explanation of every assumption is provided in Section 3.

- **Fuel Heat Deposition**. The model assumes that all heat is deposited in the fuel and no gamma heating is modeled. This simplification is based on the small impact of non-local heating on the transient, as indicated by Ref. [10], which identified gamma heating in the reflector assemblies as representing approximately 1% of the total power. Future work will be devoted to including this mechanism.

- **Control-ride driveline expansion feedback (CRDE)**. The CRDE feedback, that arises from the differential axial expansion of the control rods within the core due to changes in the core outlet temperature, is not captured by the current model. The magnitude of the feedback is highly dependent on the total control rod worth and the insertion depth of the rod banks. The reasons for the exclusion of this mechanism are (1) The rods are completely

withdrawn from the core during the ULOF scenario here modeled therefore mitigating its relative weight with respect to other feedback mechanisms. (2) The current use of a local heat deposition model does not allow to model the full heat source driving the axial expansion of the stainless-steel control rods in the core. Future work will be devoted to exploring the addition of this feedback mechanism to the current model.

- **Thermomechanics modeling approach**. The three-dimensional thermomechanical problem was deconstructed into independent two-dimensional and one-dimensional problems representing grid plate expansion,and fuel axial expansion, respectively. Therefore, three dimensional effects, such as bowing and flowering mechanisms, are not captured by the current model. These latter effects could lead to positive reactivity insertions for some assembly restraint systems, but for most designs it is assumed to be negative. Therefore, its omission would make the model more conservative.

- **Pin Thermomechanical Modeling**: In the current model, we assumed direct contact between fuel and clad for thermomechanical modeling, which is conservative from a reactivity feedback perspective. This assumption limits fuel temperature and axial displacement, resulting in lower fuel Doppler and displacement feedback. Burnup or swelling-induced expansion mechanisms are not modeled, thus ensuring conservative estimation of Advanced Burner Test Reactor dynamic response during unprotected loss of flow.

- **Inter-Assembly Heat Transfer**: Inter-assembly heat transfer is not modeled, neglecting thermal coupling between adjacent assemblies, which may affect reactor physics through temperature feedback.

- **Sodium Flow Simplification**: The model assumes well-mixed sodium in the plena. Additionally, the sodium flow path in the core is simplified by defining an effective by-pass channel encompassing all the assembly types not containing fuel and the sodium flowing between the shields and the vessel.

2.2 ABTR Core Description

The 250-MW_{th} ABTR is a metallic-fuel sodium-cooled conceptual reactor design originally developed at Argonne National Laboratory (ANL) [11]. In Ref. [1], a numerical benchmark was developed to assess the Argonne Reactor Computation suite of fast-reactor analysis codes. The core is composed of (1) 24 inner-core fuel assemblies, (2) 30 outer-core fuel assemblies, (3) 6 fuel test assemblies, (4) 3 material test assemblies, (5) 10 assemblies to provide reactivity control, (6) 78 reflector assemblies, and (7) 48 shield assemblies. Fig. 1 shows a radial view of the various assembly types, while their axial dimensions are displayed in Fig. 2. The assemblies are thermally pre-expanded in the radial direction to hot conditions, as opposed to numerically modeling the expansion. A comprehensive list of dimensions can be found in Ref. [1].

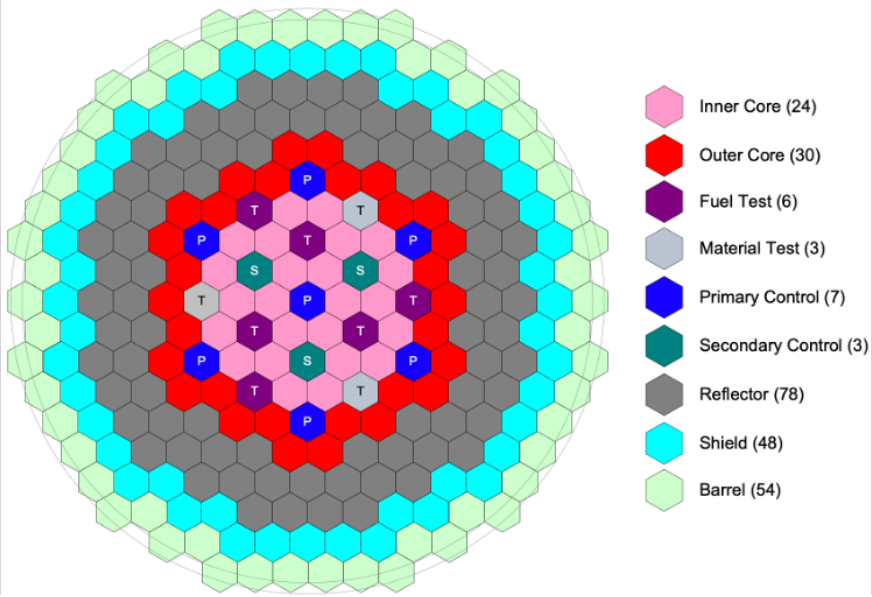

Figure 1: Radial view of the ABTR core from [1]

2.3 Transient Scenario

A ULOF transient scenario is considered a beyond-design-basis accident for sodium fast reactors. During a ULOF, the power to both the primary and secondary pumps is assumed to be completely lost, leading to a complete interruption of forced cooling in the reactor. Failure of the reactivity SCRAM mechanism is also assumed, producing a scenario in which the reactor must rely on thermomechanics and thermal-hydraulic feedback mechanisms for self-regulation.

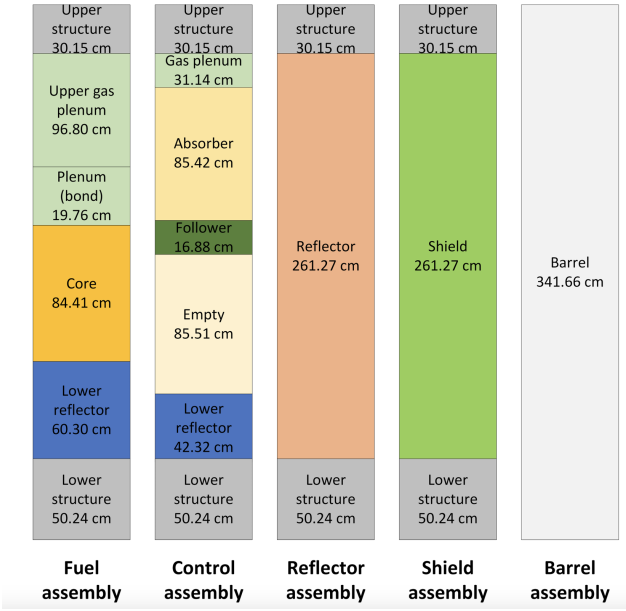

Figure 2: Axial view of the ABTR assembly types from [2].

Table 2 details the accident progression. The reactor is assumed to start out in a steady-state condition that is then maintained for 10 s before the ULOF is initiated with a sudden decrease in the primary and secondary pump heads. The pump heads are reduced up to 430 s, when they reach a value close to 0 MPa. Passive cooling is then established in the core until the transient ends at 1000 s.

Table 2: ULOF accident scenario progression.

Time (s)	Event
0 s	· Steady state · Power set to 250 MW_{th}
0–10 s	· Maintain steady-state conditions
10 s	· Start of the ULOF, assuming complete loss of power from both the primary and secondary pumps
10–430 s	· Reduce the primary and secondary pump heads to zero
430 s	· End of pump head ramp
430–1000 s	· No change in input parameters
1000 s	· End of simulation

3. ANALYSIS METHODOLOGY

In this work, a multiphysics reference plant model for the ABTR was developed using the Multiphysics Object-Oriented Simulation Environment (MOOSE)-based Comprehensive Reactor Analysis Bundle (CRAB) application. The full multiphysics model relies on four single-physics inputs that are coupled through the MultiApps system [12]: (1) a Griffin neutronics model employing MC^2-3-generated microscopic cross sections [13], (2) a BISON model simulating the radial thermal expansion of the support plate [14], (3) a BISON model simulating the axial thermal expansion of the fuel assemblies, and (4) a SAM thermal-hydraulic model simulating the reactor sodium flow [15]. An additional input, termed the intermediate sub-application, serves to transfer information between the neutronics and the sub-application. Moreover, it enables the sub-application to restart for the transient simulation. All the mesh files in this work were generated using the reactor module in MOOSE [16], eliminating the need to rely on external tools. See Sections 3.1–3.3 for a description of the single-physics models, and see Section 3.4 for an illustration of the numerical coupling scheme.

3.1 Reactor Physics Model

Griffin, a MOOSE-based reactor physics code jointly developed by INL and ANL [13], contains several numerical schemes usable for solving the neutron transport equation on structured and unstructured meshes. It also contains methods for performing steady-state, depletion, and dynamic analyses, in addition to cross-section generation capabilities for several advanced reactor types [17–19]. The present work utilizes the discontinuous finite element discrete ordinates (S_N) solver to model the neutron transport in the ABTR core. This use of neutron transport in lieu of the simpler neutron diffusion approximation stems from considerations regarding the nature of the dynamic response of SFRs. In fact, this dynamic response is mainly driven by thermomechanics-induced feedback mechanisms mediated by their effect on neutron streaming. The latter is not correctly modeled by the diffusion approximation, therefore leading to inaccurate results if diffusion is employed. Additionally, the use of neutron transport enables users to capture the effect of anisotropic scattering, which is not negligible in SFRs and can account for up to a 1000 pcm discrepancy in effective multiplication factor [20]. The neutron transport calculations are acceler-

ated by the coarse-mesh finite difference acceleration scheme in Griffin [21]. See Section 3.1.1 for a description of the approach to cross-section generation, and see Section 3.1.2 for a discussion on the spatial approximation method developed for this workscope.

3.1.1 Multigroup Microscopic Cross-Section Generation

It is well documented that Monte Carlo codes have several limitations for fast-reactors cross sections preparation, due to the importance of the higher-order scattering and the inability of current Monte Carlo methods to accurately tally higher-order scattering matrices [20, 22]. Thus, the multigroup microscopic cross sections and kinetic parameters were computed using MC^2-3 [23] and TWODANT [24]. The latest version of MC^2-3 is included in the current Griffin release.

The long neutron mean free paths inherent in fast reactor designs lead to a strong coupling of the neutron spectrum between regions throughout the core. This necessitates the computation of a fine-group neutron flux (spectrum) and flux moments from a global calculation. To reduce the computational burden, a 2D ultra-fine-group transport model is often deployed to obtain a core-wide solution [3, 23]. In this work, we account for the leakage effect by relying on a 2D ultra-fine-group transport solution from TWODANT [24]. The isotopic compositions are based on the beginning-of-equilibrium core. The evaluated nuclear data library cross sections were based on ENDF/B-VII.r1.

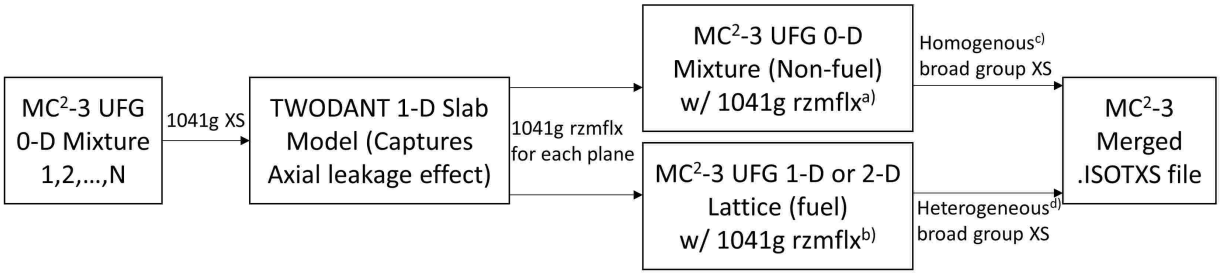

Figure 3: Fast reactor cross-section preparation [3].

At the time the present work was initiated, no fully developed SFR workflow existed in Griffin, so a set of Python scripts was deployed to mimic the SFR workflow reflected in Figure 3. The current version of Griffin incorporates this specialized workflow for SFRs; nonetheless, a cursory

explanation is included herein. Griffin did automatically convert the cross-section data from the MC^2-3 ISOTXS format into the Griffin ISOXML format, and this capability was leveraged in the Python scripts, which perform the following tasks:

1. Azimuthal homogenization of core composition by core ring to produce an effective R-Z model.

2. Preparation of ultra-fine-group cross sections for various assembly types using MC^2-3 and energy condensation to 1,041 groups. Fuel and control assemblies rely on 1D calculations to resolve inter-assembly self-shielding effects. Other regions use a homogenized approach.

3. Execution of the TWODANT transport solution—with 1,041 energy groups within the MC^2-3 input—to produce the flux and flux moments.

4. Execution of the MC^2-3 homogenization and condensation, using the ultra-fine-group cross sections and the flux and flux moments.

5. Addition of delayed neutron data into the ISOXML library, based on DLAYXS files produced by MC^2-3.

6. Merger of auxiliary ISOXML files into a final ISOXML master library containing all needed isotopes and all state points.

The microscopic cross sections were prepared at the state points shown in Table 3. The ANL9 group structure used to generate the cross sections is reflected in Table 4.

Table 3: Temperature tabulation of the ABTR microscopic cross sections.

Region	Temperatures [K]
Fuel	600.0, 805.65, 855.65, 905.65, 955.65, 1155.65, 1200.0
Non-fuel	600.0, 805.65, 855.65, 905.65, 955.65, 1155.65

3.1.2 Neutronics Method

Three approaches have traditionally been employed for neutronics modeling of SFRs: (1) the spatially homogeneous approach, in which, by taking advantage of the long mean free paths of neutrons in fast reactors, cross sections are computed assembly-wise and are functionalized with

Table 4: Broad group structure.

Group	Upper Energy Boundaries [eV]
1	1.4191E+07
2	2.2313E+06
3	8.2085E+05
4	1.8316E+05
5	4.0868E+04
6	9.1188E+03
7	2.0347E+03
8	4.5400E+02
9	5.0435E+00

respect to the mechanical deformation; (2) the fully heterogeneous (FH) approach, in which the reactor geometry is modeled in the most accurate way possible within the limitations of the meshing system; and (3) the duct-heterogeneous approach, in which the fuel, clad, and flowing coolant are homogenized within each fuel assembly, while the duct and external stagnant sodium are explicitly modeled [25]. As with the duct-heterogeneous approach, the RH approach adopted herein resides at an intermediate spatial resolution level between the homogeneous and the FH approaches. Considering that each reactor component must be able to be explicitly deformed to properly capture the differential material expansion and the associated feedback effects, the ring-heterogeneous (RH) approximation retains the heterogeneity between each component yet still significantly reduces the number of elements. In this respect, the RH approximation resembles the duct-heterogeneous approximation, with all the components in a given assembly being homogenized, except for in the duct region. By retaining the heterogeneities in the duct region, the duct-heterogeneous approximation can still explicitly model the radial deformation of assemblies. However, it is limited in regard to simulating the axial deformation of unit components such as fuel or control rod drivelines, and must rely on the cross-section functionalization with respect to the deformation in order to simulate it. The RH approximation is intended to eliminate such limitations.

The idea behind RH approximation is to cast an array of pin cells into the "bands" of materials and components constituting the pin cells (e.g., fuel, cladding, and coolant), yet still preserve their volumes. In a hexagonal geometry, the pin cells along each hexagon will be smeared into bands that resemble rings, which is how this approximation scheme got its name. Fig. 4 schematically

illustrates the two RH approximations investigated in this work: the exact RH approximation and the simplified ring-heterogeneous (SRH) approximation. The exact RH approximation (referred to hereafter as simply "the RH approximation") preserves the "topology" of the components. In Fig. 4, for instance, the topology of the fuel that is centered and surrounded by cladding and coolant is conserved. The SRH approximation, however, makes a more aggressive approximation in order to minimize the number of elements by clustering the clad into a single band per ring, instead of splitting it into two bands per ring.

Table 5 shows the spatial approximation effect when moving from FH to RH and SRH meshes on a single 2D ABTR fuel assembly. It is seen that RH can reduce the number of elements from FH by 40 times. SRH cuts the number of elements from RH down by an additional third, but makes the fuel bands more centered than in the actual assembly configuration. Furthermore, one side of the fuel band will come into direct contact with the sodium, while the other will run up against a thicker strip of cladding, thus somewhat altering the neutronic characteristics of the problem. Section 4.1 investigates the impact of RH and SRH on model accuracy in terms of absorption, fission rate, and multiplication factor.

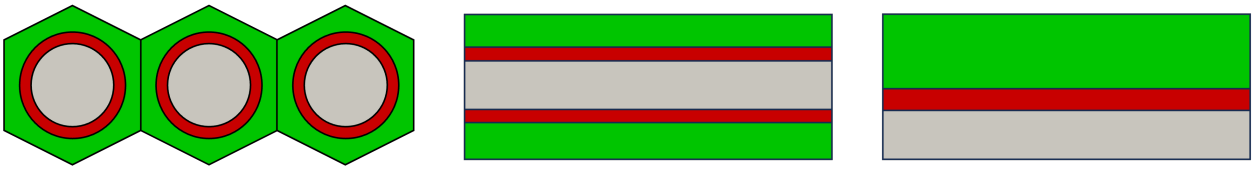

Figure 4: Schematic diagram of the exact RH (middle) and SRH (right) approximations of a FH (left) geometry.

The local decay heat deposition is modeled by assuming that the spatial distribution of the decay heat coincides with the steady-state fission source distribution. The decay heat spatial distribution is normalized to the total value of decay power pre-computed via a Serpent full-core calculation. The total decay heat curve used in this work is displayed in Fig. 5 as a function of time.

3.2 Thermomechanics

BISON, a MOOSE-based finite element fuel performance code developed at INL [14], has been verified and validated for a variety of fuel types, including metallic fuels. In the present work,

Table 5: Comparison of FH, RH, and SRH meshes on a 2D ABTR fuel assembly.

Mesh	FH	RH	SRH
Geometry	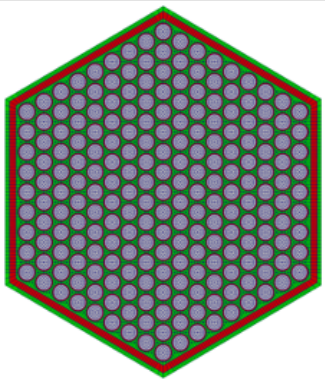	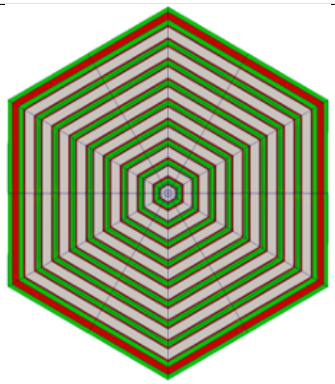	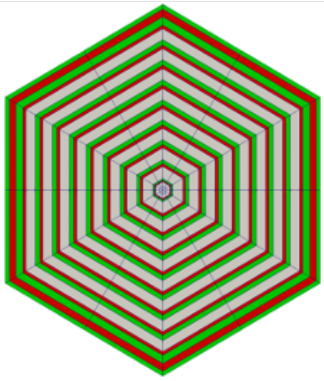
# Elements	22,056	546	354

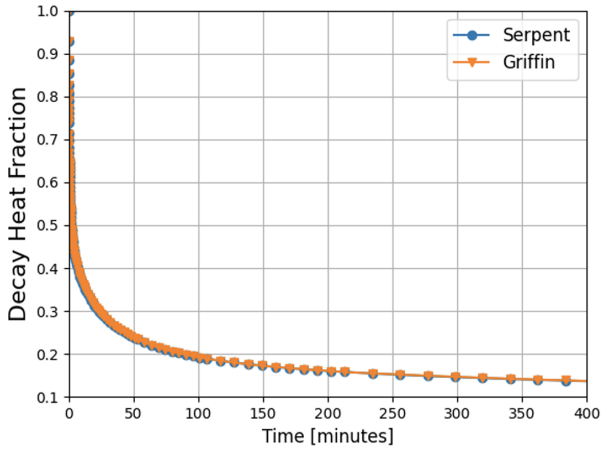

Figure 5: Pre-computed total decay heat as a function of time.

BISON was used to solve the thermomechanical equations describing the radial and axial displacement fields in the ABTR core. At this modeling stage, the 3D mechanical problem was deconstructed into a set of independent 2D and 1D problems. The 2D problem describes the radial expansion of the support plate and the consequent assembly pitch change. For the sake of simplifying this problem, the pin thermomechanical model was radially pre-expanded to hot dimensions by using the hot dimensions reported in Ref. [1], rather than numerically modeling the assemblies' radial expansion. Sixty independent 2D R-Z axisymmetric pin thermomechanical problems were instead used to model the axial fuel expansion. Non-uniform radial expansion resulting in bowing and flowering was not modeled. This led to a conservative estimate for the reactor reactivity response, as the associated negative reactivity feedback was not modeled.

3.2.1 Fuel Thermal Axial Expansion

The fuel thermal axial expansion was simulated by using a representative pin for each different assembly, instead of resorting to a FH assembly model. This simplification is based on the relatively small radial power gradient in each assembly, caused by the large mean free paths of neutrons in SFRs. The mesh for the representative pins, shown in Fig. 6, is composed of three blocks/subdomains: (1) fuel, (2) clad, and (3) axial reflector. For the fuel, the constitutive relations available in Bison for the UPuZr fuel and the HT9 were used for the clad and axial reflector. No density evolution, including burnup and swelling effects, was modeled. Additionally, the fuel and clad were in perfect contact (no sodium bond was modeled). Both these simplifications were made to generate a conservative system feedback response. In fact, the limitation of the axial expansion of the fuel pin, achieved through clad resistance and by only accounting for thermal expansion, restricted the axial fuel displacement and thus the associated negative neutronic feedback. Both the heat conduction and displacement equations were solved in the same BISON input. The mechanics relied on the finite strain approximation, as the expected displacement magnitude was on the order of centimeters [1]. Boundary conditions were imposed to avoid any rotation and translation of the pin. Additionally, the heat conduction equation was solved by imposing convective boundary conditions at the clad external surface. The sodium temperature and heat transfer coefficient used to define the convective boundary condition were obtained from the SAM full-core model through transfers (see Section 3.4 for additional information on the coupling strategy and transfers).

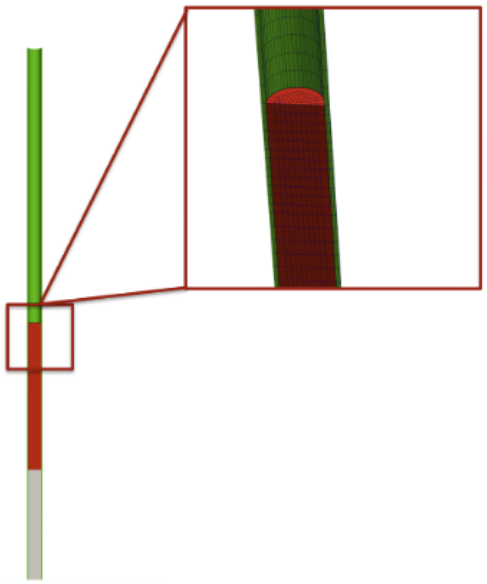

Figure 6: Mesh for the pin thermomechanical simulation. Each color represents a different block in the mesh—green: cladding, white: reflector, red: fuel.

3.2.2 Support Plate Radial Expansion

The BISON support plate models the radial cross section of the 3D stainless-steel support plate. The geometrical domain for the support plate is shown in Fig. 7.a. The hexagonal net, visible in the center of the plate, is the area on which the ducts and assemblies are positioned. As explained in Section 3.2.1, the assemblies and ducts are pre-expanded radially, and the pitch variation during the transient is dictated by the support plate radial expansion. As for the pin thermomechanical problem, both the heat conduction equation in the steel and the displacement equations for finite strain formulation are solved in a single input. Fig. 7.a displays the spatial domain on which the equations are solved. The constitutive relations for the thermomechanical properties of stainless steel 316 were used in this work. Use of a 2D mesh in lieu of a full 3D model was based on the lack of axial specifications for the support plate at the time when this model was created. The plate can, in fact, have a highly complicated axial structure, as shown in Fig. 7.b. However, to be able to match the thermal inertia associated with the 3D structure, two multipliers acting on the density are defined in the BISON input. These multipliers are used to act on the heat capacity (i.e., ρc_p) and, therefore, the characteristic thermal time constant of the system, τ, defined as:

$$\tau = \frac{\rho c_p V}{hS}, \tag{1}$$

where ρ is the density, c_p is the specific heat, V is the steel volume, S is the heat exchange surface between the steel and sodium, and h is the heat transfer coefficient. The heat exchange between the steel and sodium is modeled through a convective boundary condition:

$$-\lambda \frac{\partial T}{\partial s} = h(T - T_{Na}), \tag{2}$$

where λ is the thermal conductivity of the steel, T is the temperature, ∂s is the increment orthogonal to the surface of the stainless steel, h is the heat transfer coefficient between sodium and steel, and T_{Na} is the sodium temperature. It is assumed that h and T_{Na} are the same across the entire support plate, due to good sodium mixing in the inlet plenum.

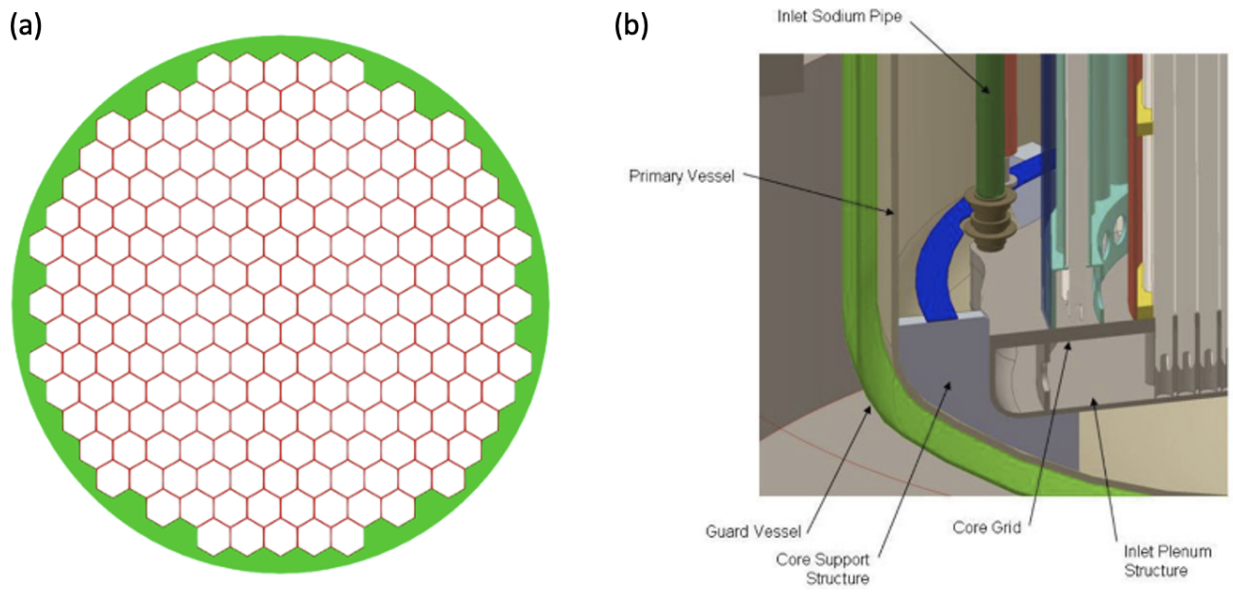

Figure 7: (a) Support plate mesh and (b) Rendering of realistic support plate 3D structure (figure reproduced from [4]).

3.3 Thermal Fluids

SAM is an ANL-developed system code that specializes in simulating the thermal hydraulics in non-light-water reactors. SAM, which enables users to perform whole-plant transient analyses, was recently extended to model general multi-dimensional single-phase flows. In the present work, SAM was used to model the sodium flow in the ABTR. The model was based on specifications in Refs. [2, 26]. Fig. 8 displays a schematic of the system as modeled in SAM. The main components comprising the model are the (1) core, (2) inlet plenum, (3) outlet plenum, (4) pool, (5) three heat exchangers (one secondary-loop heat exchanger and two primary-loop heat exchangers), and (6) two pumps. A description of the modeling approach applied to each of these component types is presented below.

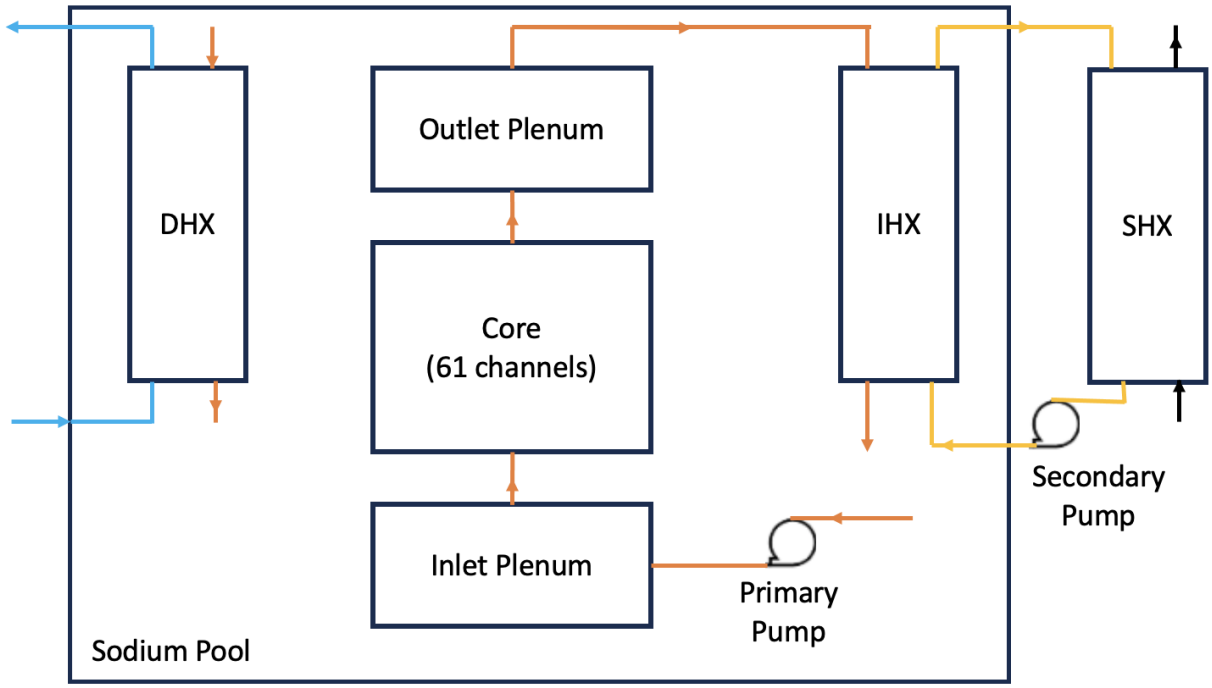

Figure 8: Schematics of the ABTR thermal-hydraulics model.

1. The sodium flow in the core was modeled using 61 equivalent channels connected through the inlet and outlet plenum. Sixty of these channels were used to represent the flow in each fuel assembly (i.e., one channel per assembly), and each axial section of the fuel equivalent channels consisted of three axisymmetric domains: (1) fuel, (2) clad, and (3) flowing sodium.

We assumed that the sodium was in thermal equilibrium with the duct enclosing the assembly. The additional channel in the core model was used to represent the sodium flow in the non-heated assemblies. The heat transfer coefficient was computed in SAM by using the Kazimi-Carelli correlation, which is the standard correlation for describing the heat transfer for pin bundles cooled by liquid metals in the regime of interest.

2. The inlet plenum was modeled using a *PBVolumeBranch* object, a 2D object featuring an associated volume, width, and height. The inlet plenum receives the primary pump output and redistributes the sodium across the 61 channels composing the core, based on the area and the pressure losses involved.

3. The outlet plenum was modeled using a *PBLiquidVolume* component, due to both sodium and cover gas being present. The outlet plenum takes the core outlet information as an input, and the output is provided tothe intermediate heat exchanger.

4. The pool was modeled using a *PBLiquidVolume* component, due to the presence of both sodium and cover gas. The cold pool receives the sodium flow as an input from the primary pumps, and provides the output to the DRACS heat exchanger.

5. The three heat exchangers (i.e., the DRACS, intermediate, and secondary heat exchangers) were modeled using the *PBHeatExchanger* component, and were all assumed to work in counter flow.

6. The primary and secondary pumps were modeled using the *PBPump* components. The pump heads can be user-specified. In this model, the pump heads for both the primary and secondary pump are externally imposed through auxiliary functions, and they dictate the mass flow rate decrease that drives the transient.

3.4 Coupling Strategy

The coupling scheme, illustrated in Fig. 10, remains valid for each time step of the transient. For steady-state conditions, the coupling scheme is repeated at each Picard iteration and is stopped once the effective multiplication factor converges within 10^{-8} in absolute tolerance. This stringent

criterion was chosen for the tolerance in order to enforce convergence of the thermal and displacement scalar fields (*i.e.*, temperature and components of displacement).

As seen in Fig. 10, the Griffin neutronics model described in Section 3.1 is the master application, and is used to compute the power density distribution, as denoted by P_d in Fig. 10. The power density is then transferred to the intermediate sub-application, which is utilized to transfer data from the neutronics to the Level-2 sub-applications, and vice versa. In addition, the intermediate sub-application is utilized to restart the Level-2 sub-applications from the final coupled steady-state solution, and to perform the transient ULOF calculations. This intermediate sub-application will be eliminated in future versions of the model once the checkpoint restart capability is fully merged and tested in Griffin. From a meshing standpoint, the intermediate sub-application is a radially coarser representation of the ABTR than that used to solve the discretized neutron transport equation. Fig. 9 juxtaposes the mesh used for the transport solution and the one used for the intermediate sub-application.

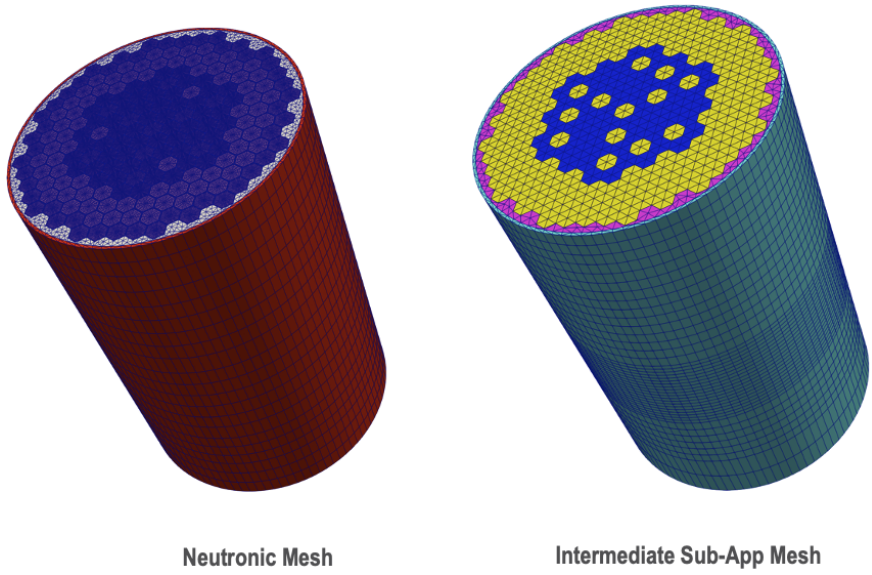

Figure 9: Juxtaposition of the neutronic and sub-application meshes.

P_d is passed down to both the Level-2 sub-applications and assigned to the correct pin, based on the location in the core. The SAM thermal hydraulic model described in Section 3.3 then computes the sodium temperature (T_{Na}), heat transfer coefficient (h), and sodium density (ρ_{Na}). These quantities are then transferred back to the intermediate sub-application, which sends T_{Na} and h to the 60 instances of the pin thermomechanics sub-application models described in Section 3.2.1.

From the pin thermomechanics calculations, the fuel temperature (T_f), axial reflector temperature (T_r), and clad temperature (T_c) are obtained, along with the corresponding axial components of the displacement fields, here denoted as ϵ_z^f, ϵ_z^r, and ϵ_z^c, respectively. Picard iterations between the fluid and thermomechanics simulations are performed until convergence is achieved. The intermediate sub-application then sends back the temperature, displacement, and sodium density fields to the neutronics, where cross sections are updated based on the values of these fields. The neutronics is finally coupled to the support plate thermomechanics by transferring the sodium temperature and the heat transfer coefficient at the inlet plenum. The support plate thermomechanics model described in Section 3.2.2 computes the radial displacement field, which is composed of the x- and y-components of the displacement field, here denoted as ϵ_x and ϵ_y, respectively.

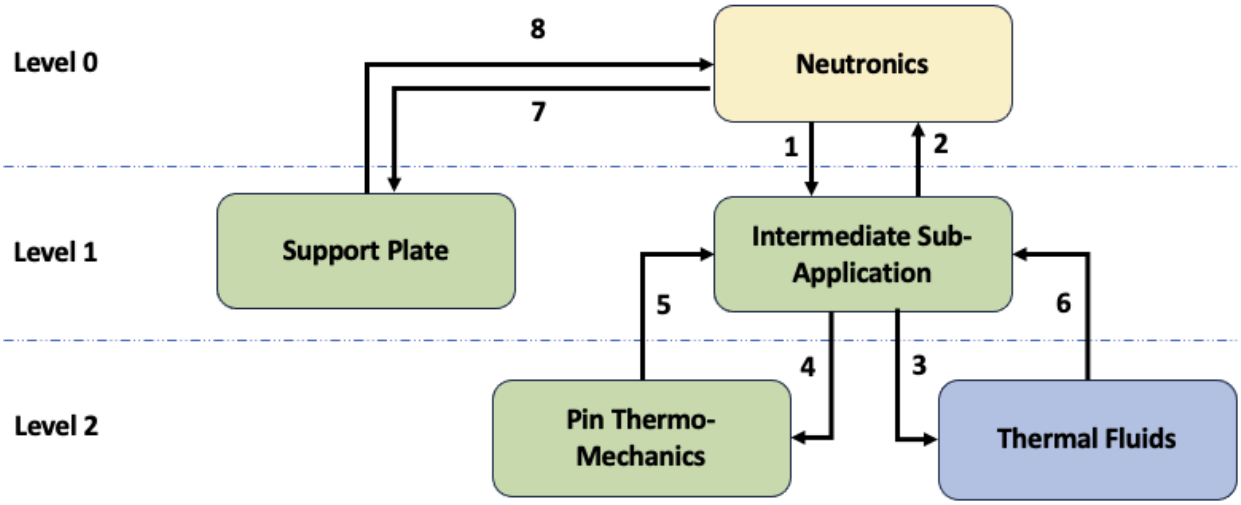

Figure 10: Coupling strategy for the ABTR model.

Table 6: Transferred quantities within the coupling scheme. The transfer numbers refer back to the labels used in Fig. 10.

Transfer Number	Transferred Quantities
1	P_d
2	T_f, T_r, T_c, ϵ_z^f, ϵ_z^r, ϵ_z^c, T_{Na}, ρ_{Na}, h_{Na}
3	P_d
4	P_d
5	T_f, T_r, T_c, ϵ_z^f, ϵ_z^r, ϵ_z^c,
6	T_{Na}, ρ_{Na}, h_{Na}
7	T_{Na}, h_{Na}
8	ϵ_x, ϵ_y

4. RESULTS

This section is divided into three subsections. In Section 4.1, the full-core reactor physics model is verified against the reference Serpent calculations. Sections 4.2 and 4.3 report the results for the full-core steady-state and transient coupled calculations.

4.1 Neutronics Model Verification

This section presents the verification of the Griffin standalone neutronics calculation for both the single-assembly and full-core ABTR models. In all the calculations, Griffin employed MC^2-3-generated nine-group cross sections (i.e., the ANL9 group structure) in combination with the first-order discontinuous finite element S_N method, with two polar angles and six azimuthal angles per octant (Gauss-Chebyshev angular quadrature). For each case, the fission and absorption reaction rates were compared with Serpent, along with the eigenvalues. For the 3D full-core problem, the reactivity coefficients and kinetics parameters were also verified. Here, the absorption reaction excludes fission; namely, it is the sum of all reactions that do not produce neutrons. The reaction rate distributions are normalized such that the volume average becomes unity, and their errors are given as absolute differences in percent. Unless specified, the temperature is set to 855.65 K (i.e., the average fuel operating temperature according to Ref. [1]), and the geometries are in the hot dimension.

4.1.1 2D Assemblies

For 2D single-assembly problems, we compared the eigenvalues and ring-wise fission and absorption reaction rates of Serpent, FH, RH, and SRH. The Serpent calculations employed 50 inactive and 200 active cycles, with a million particles per cycle, resulting in 200 million active histories. For Serpent and Griffin, Table 7 reports the eigenvalues of the three types of fuel assemblies under the three different types of meshes. Fig. 11 illustrates the ring-wise fission reaction rate errors of FH vs. Serpent, and Fig. 12 presents the errors of RH and SRH vs. FH. Figs. 13 and 14 present the corresponding data on absorption reaction rates. This serves to separate the baseline errors against Serpent due to cross sections, discretizations, and the RH approximation.

Serpent and Griffin show good agreements in regard to the 2D single-assembly problems. The

eigenvalue errors of FH vs. Serpent do not exceed 20 pcm. The maximum ring-wise fission reaction rate error is less than 0.1%, and 0.15% for absorption. Both these values are negligible, confirming the baseline accuracy of Griffin when validated against Serpent. The RH approximation yields eigenvalues nearly identical to those of FH, with errors of less than 5 pcm, while SRH presents errors of 40–60 pcm. For the fission reaction rate, both RH and SRH show negligible error values, the maximum being only around 0.1%. For the absorption reaction rate, however, SRH does present the highest error value (i.e., over 0.6%), though that of RH is below 0.1%, which is considered the reason for the larger SRH eigenvalue errors. The error behavior difference when comparing the fission and absorption reaction rates is thought to stem from the role of U-238, whose number density still accounts for over 60% of the fuel. The fission reaction rate presents a very flat distribution, as it is dominated by fast fission. On the other hand, in the absorption reaction rate, the resonance absorption and self-shielding of U-238 becomes non-negligible. Self-shielding is strongly affected by geometry, and thus SRH, which fails to preserve the topology of the original geometry, incurs larger errors than RH—especially in terms of absorption reaction rates. Still, the degrees of error for SRH are considered acceptable in practical terms.

Table 7: Comparison of 2D assembly eigenvalues (uncertainties and errors in pcm).

Model	Inner Fuel	Middle Fuel	Outer Fuel
Serpent	1.55311 ($\pm$ 3)	1.39235 ($\pm$ 3)	1.71965 ($\pm$ 3)
FH	1.55326 (15)	1.39217 (-18)	1.71978 (13)
RH	1.55331 (20)	1.39222 (-13)	1.71982 (17)
SRH	1.55374 (63)	1.39275 (40)	1.72021 (56)

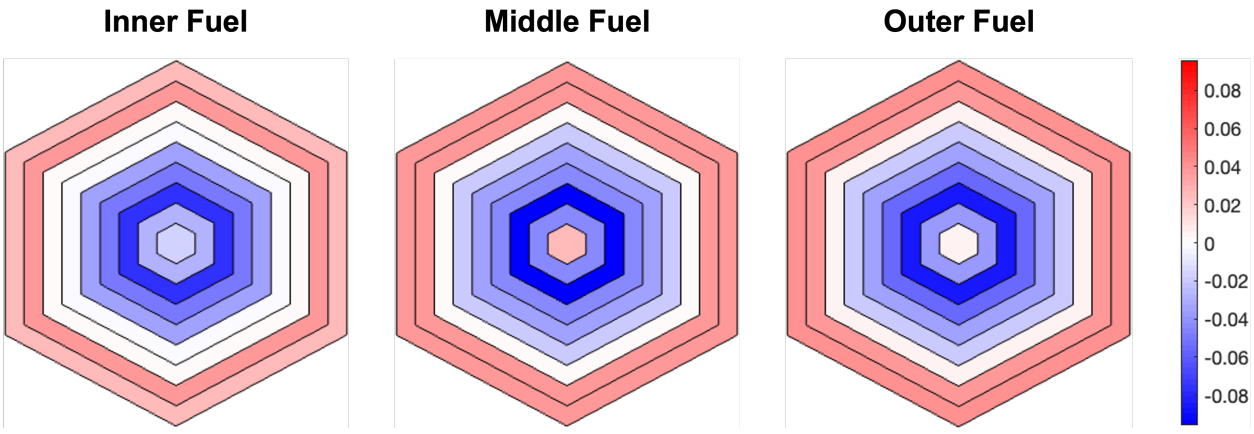

Figure 11: Ring-wise fission reaction rate errors (%) of FH vs. Serpent, for the 2D assemblies.

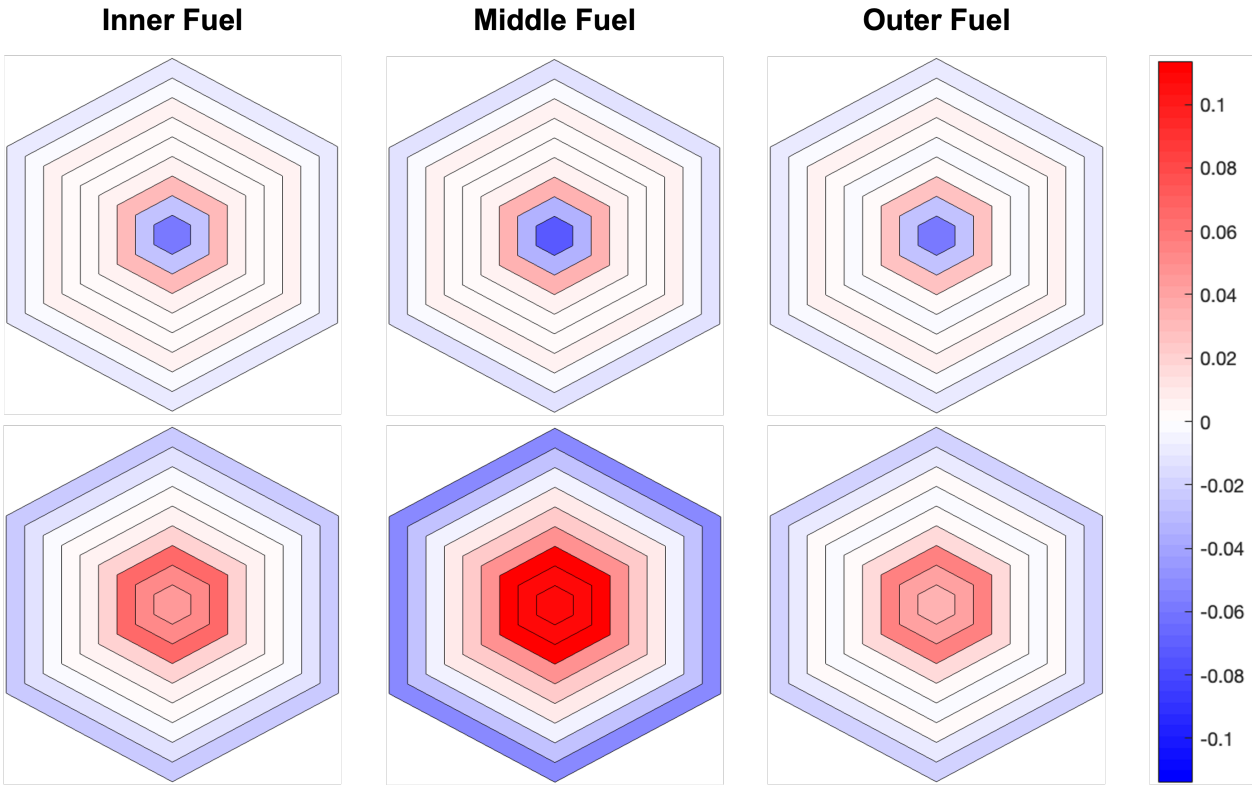

Figure 12: Ring-wise fission reaction rate errors (%) of RH (top) and SRH (bottom) vs. FH, for the 2D assemblies.

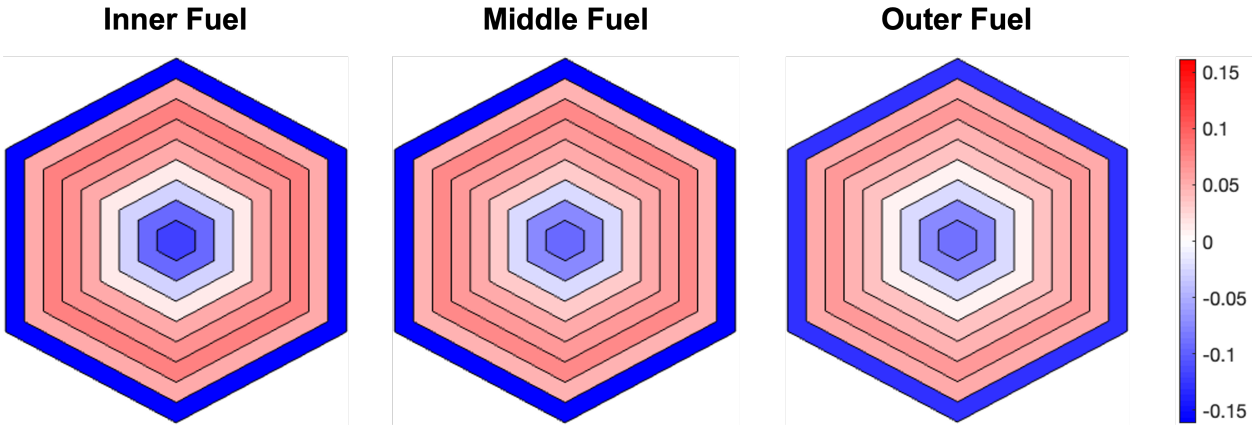

Figure 13: Ring-wise absorption reaction rate errors (%) of FH vs. Serpent, for the 2D assemblies.

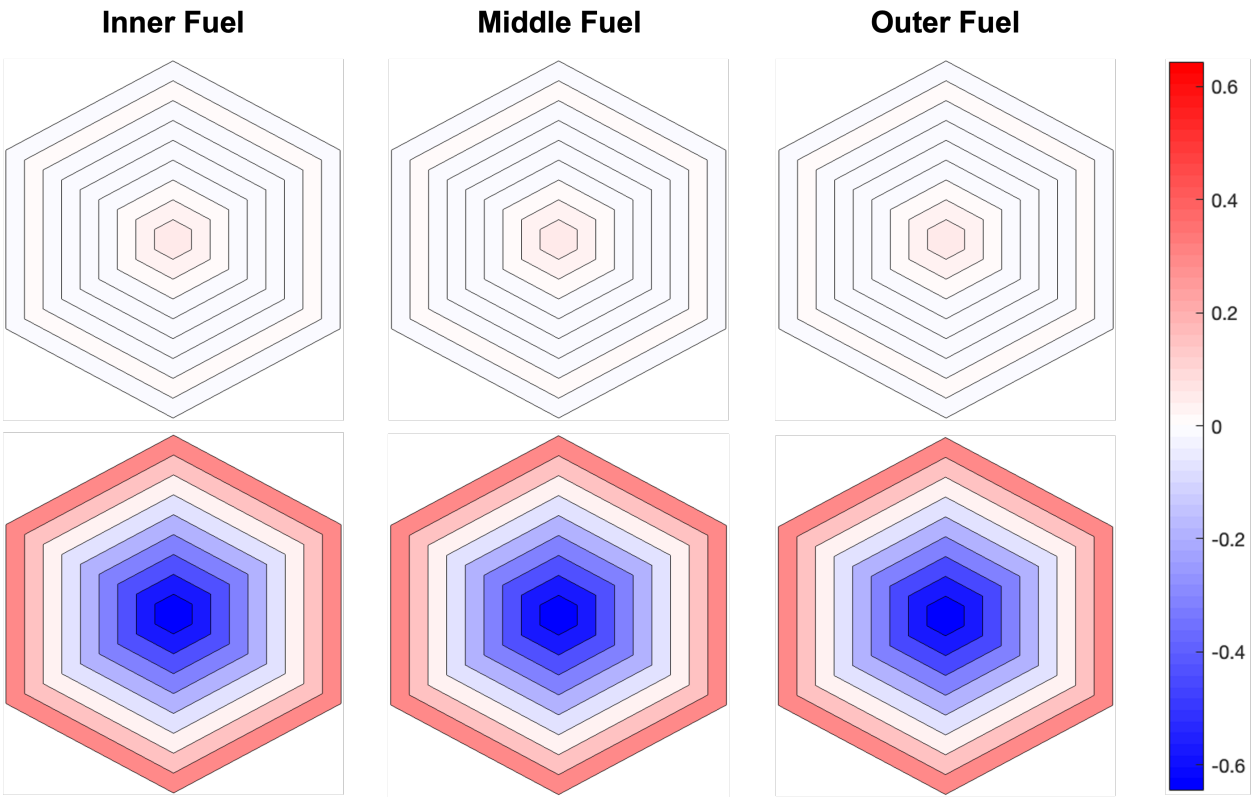

Figure 14: Ring-wise absorption reaction rate errors (%) of RH (top) and SRH (bottom) vs. FH, for the 2D assemblies.

4.1.2 3D Assemblies

For 3D single-assembly problems, we compared the eigenvalues and radially integrated plane-wise fission and absorption reaction rates in the active core region when using Serpent, FH, RH, and SRH. As the axially integrated ring-wise reaction rates present a trend similar to that seen in the 2D single-assembly cases, they are not repeated here. Just as before, the reaction rate errors are presented separately for FH vs. Serpent, and RH and SRH vs. FH. The Serpent calculations employed 50 inactive and 1,000 active cycles, with a million particles per cycle, generating a billion active histories. For Serpent and Griffin, Table 8 reports the eigenvalues of the three types of fuel assemblies under the three different types of meshes. Fig. 15 gives the radially integrated plane-wise fission reaction rate errors of FH vs. Serpent, and Fig. 16 shows the errors of RH and SRH vs. FH. Figs. 17 and 18 illustrate the corresponding absorption reaction rate data.

Table 8: Comparison of 3D assembly eigenvalues (uncertainties and errors in pcm).

Model	Inner Fuel	Middle Fuel	Outer Fuel
Serpent	1.35142 ($\pm$ 2)	1.21521 ($\pm$ 2)	1.50559 ($\pm$ 2)
FH	1.34932 (-210)	1.21408 (-113)	1.50269 (-290)
RH	1.34935 (-207)	1.21414 (-107)	1.50272 (-287)
SRH	1.34973 (-169)	1.21464 (-67)	1.50305 (-254)

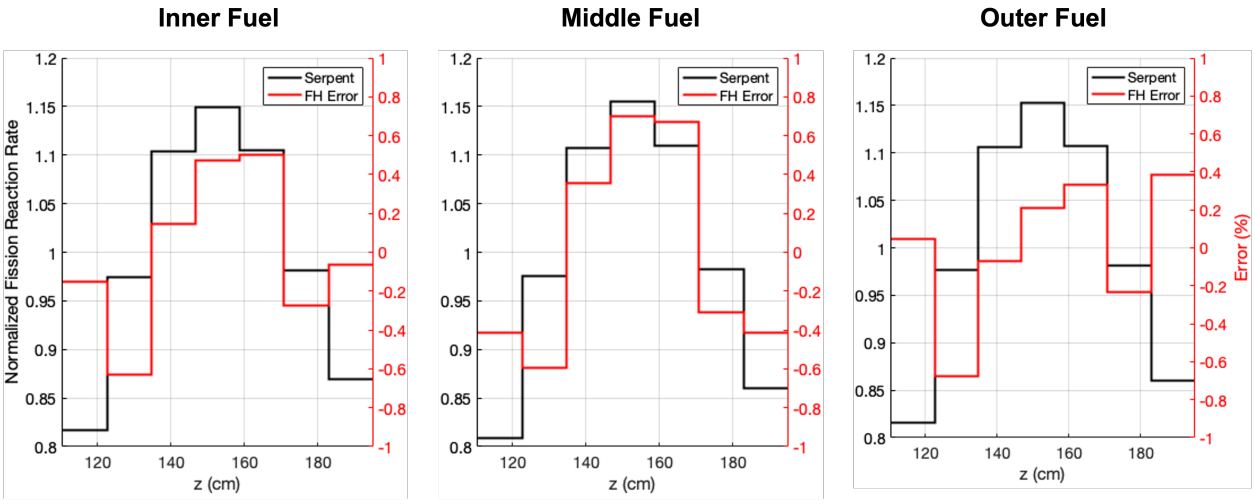

Figure 15: Radially integrated plane-wise fission reaction rates of Serpent and the errors (%) of FH vs. Serpent, for the 3D assemblies.

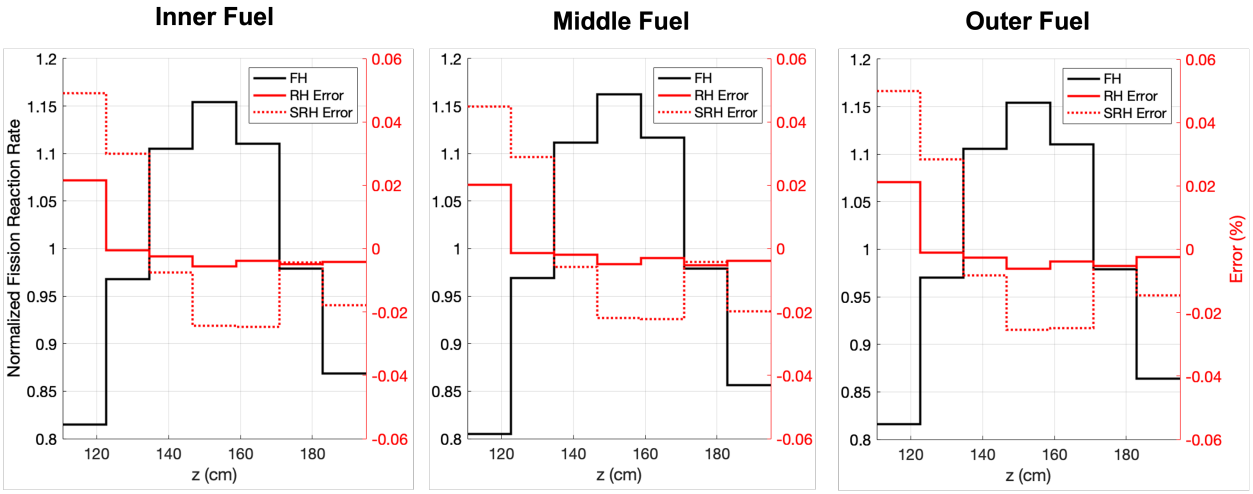

Figure 16: Radially integrated plane-wise fission reaction rates of FH and the errors (%) of RH and SRH vs. FH, for the 3D assemblies.

Compared to the 2D single-assembly cases, a wider difference was seen between the baseline errors and the errors generated in Serpent. This difference arose due to the axial leakage effect

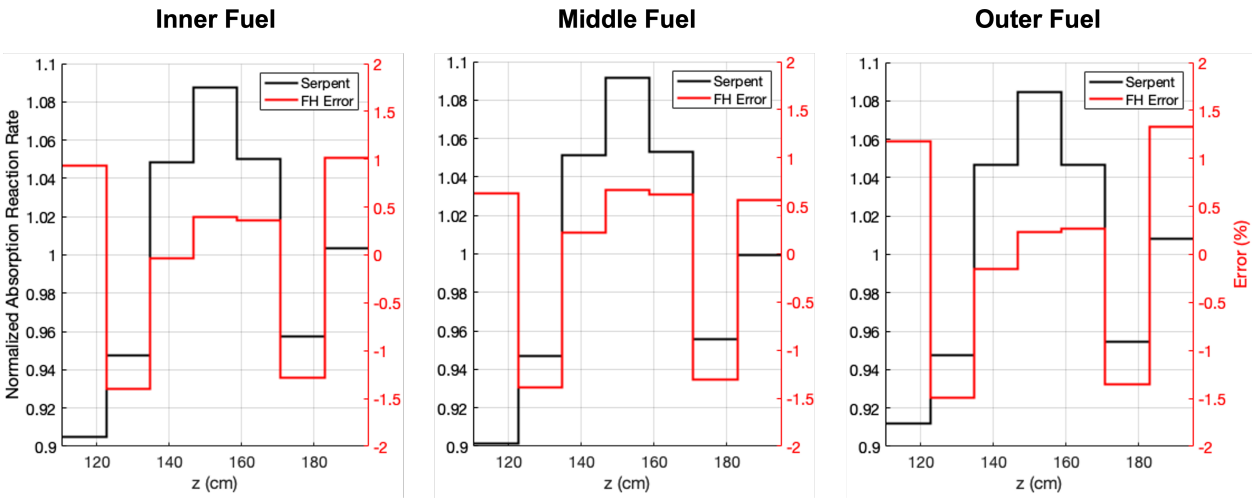

Figure 17: Radially integrated plane-wise absorption reaction rates of Serpent and the errors (%) of FH vs. Serpent, for the 3D assemblies.

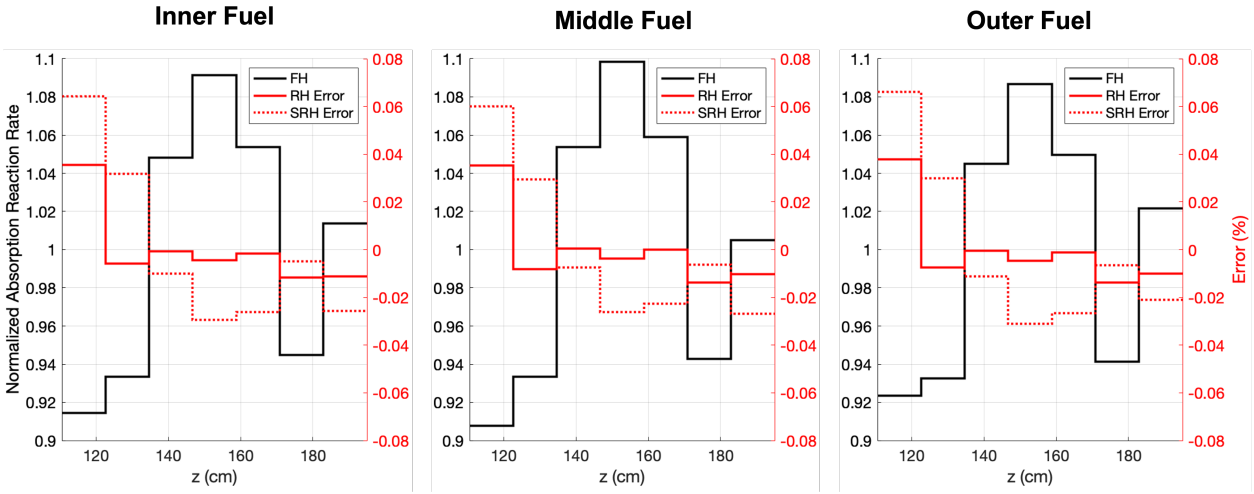

Figure 18: Radially integrated plane-wise absorption reaction rates of FH and the errors (%) of RH and SRH vs. FH, for the 3D assemblies.

Depending on the assembly type, FH presents eigenvalue errors ranging from -110 to -290 pcm. The plane-wise reaction rates show errors of up to 0.8% for fission and 1.5% for absorption. This implies that the cross sections still need to be improved for 3D calculations. However, the RH approximation itself remains valid. The eigenvalues exhibit a trend very similar to that seen in the 2D single-assembly cases: RH yields almost the same eigenvalues as FH, while SRH shows positive biases on the order of tens of pcm. Furthermore, the reason for the larger errors in SRH is identical to what is seen in the 2D single-assembly cases. In terms of plane-wise reaction rates, although SRH tends to produce larger errors, the magnitude of these errors nonetheless remains

negligible. Thus, neither RH nor SRH are considered to have a meaningful impact on the axial solutions.

4.1.3 2D Full Core

For the 2D full-core case, the RH and SRH eigenvalues and ring-wise fission and absorption reaction rates in the fuel assemblies are compared against the FH results. The set of cross sections used for this case originated from the 3D full-core case. In other words, the set was not generated with the proper flux spectra for the 2D core. Thus, the results are not compared with Serpent. Instead, this case is intended to validate RH and SRH vs. FH in the actual core configuration, on the same cross-sectional basis. The FH mesh contains 4,291,772 elements, whereas the RH and SRH meshes only contain 61,444 and 47,872, respectively. At minimum, this represents the number of elements being reduced by a factor of 70. Table 9 presents the eigenvalues of the FH, RH, and SRH calculations, and Figs. 19 and 20 show the ring-wise fission and absorption reaction rate errors of RH and SRH vs. FH.

Table 9: Comparison of 2D full-core eigenvalues (errors in pcm).

Model	FH	RH	SRH
Eigenvalue	1.23811	1.23792 (-19)	1.23928 (117)

RH showcases almost exact agreement with FH in all the observed quantities. The eigenvalue error is only -19 pcm, and the degrees of error in the reaction rates remain at levels comparable to the single-assembly problems: the maximum fission and absorption reaction rate errors are 0.10% and 0.08%, respectively, and the corresponding root mean square errors (RMSEs) are 0.02% and 0.01%, respectively—values that are completely negligible. This implies that RH is unaffected by environmental effects. On the other hand, SRH exhibits larger errors overall. The eigenvalue error exceeds 100 pcm, and the absorption reaction rate error is close to 1% in the maximum whereas the RMSE is 0.30%. The fission reaction rate error is lower—a maximum error and RMSE of 0.34% and 0.16%, respectively—owing to the fact that fast fission is not much affected by self-shielding. However, a global in/out tilt is observed in the error distribution, indicating that SRH is affected by environmental effects, unlike RH. In fact, while the errors seem large in a relative sense when compared against RH, their magnitudes are not, in and of themselves, generally considered sig-

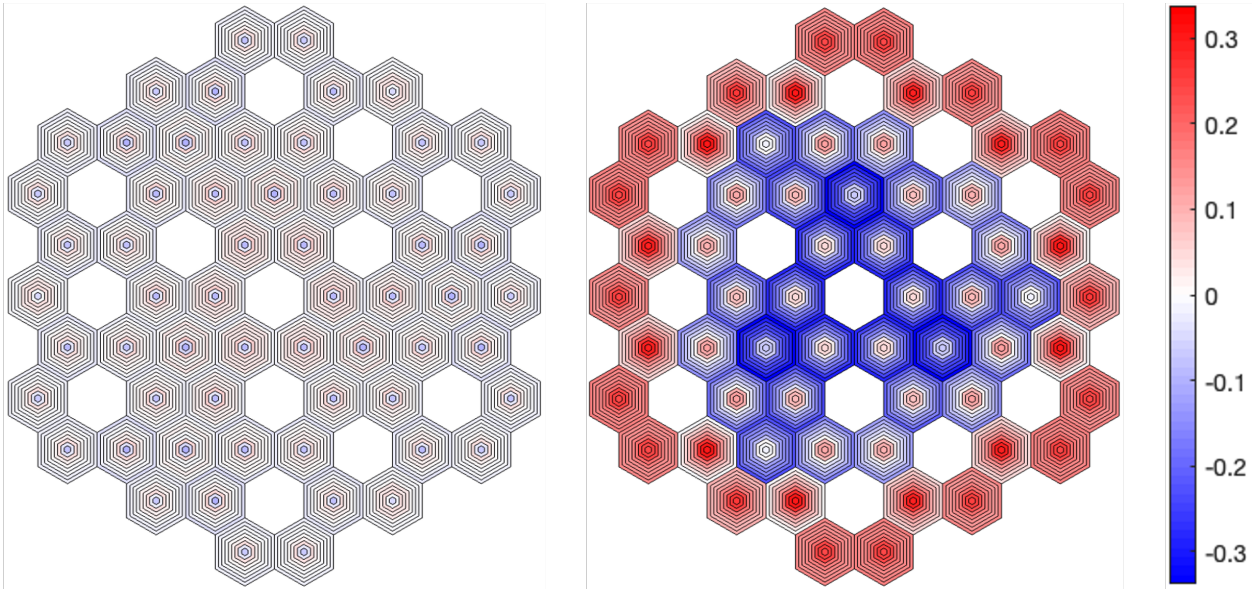

Figure 19: Ring-wise fission reaction rate errors (%) of RH (left) and SRH (right) vs. FH, for the 2D full core.

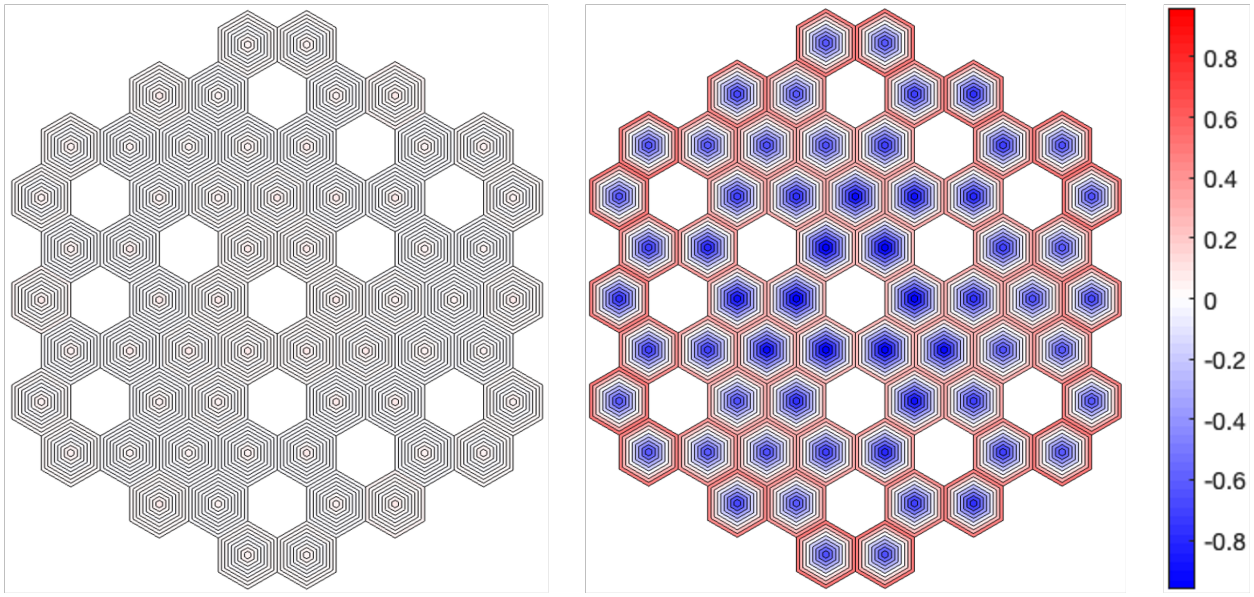

Figure 20: Ring-wise absorption reaction rate errors (%) of RH (left) and SRH (right) vs. FH, for the 2D full core.

nificant. However, these errors can be amplified under more challenging conditions (e.g., rodded, transient, or multiphysics conditions), so more thorough investigations will be required in order for SRH to be utilized under such "irregular" conditions.

4.1.4 3D Full Core

For the 3D full-core case, the computational cost of the FH calculation is prohibitive, so the RH and SRH solutions are directly compared with the Serpent solutions. Griffin was parallelized with 200 cores of Intel Xeon Gold 6148 CPUs. The RH and SRH meshes contained 1,467,456 and 1,148,928 elements, respectively, resulting in respective runtimes of 28.8 and 24.3 minutes. The Serpent calculations employed 100 inactive and 1,000 active cycles, with 10 million particles per cycle, ultimately generating 10 billion active histories.

Table 10 shows the eigenvalues of the Serpent, RH, and SRH calculations, and Figs. 21 and 22 illustrate the reference axially integrated ring-wise fission and absorption reaction rates of Serpent and the errors of RH and SRH vs. Serpent. Because of the vastness of the data, the detailed local 3D ring-wise reaction rates are not presented. Instead, the maximum errors and RMSEs of the local 3D—as well as the axially integrated 2D—ring-wise reaction rates are reported in Table 11. Lastly, Fig. 23 presents the reference radially integrated plane-wise fission and absorption reaction rates of Serpent in the active core region, along with the errors of RH and SRH vs. Serpent. Note that for the ring-wise reaction rates, only the fuel assemblies are of interest, while the plane-wise reaction rates include all the assemblies.

Table 10: Comparison of 3D full-core eigenvalues (uncertainties and errors in pcm).

Model	Serpent	RH	SRH
Eigenvalue	1.03288 ($\pm$ 1)	1.03388 (100)	1.03554 (266)

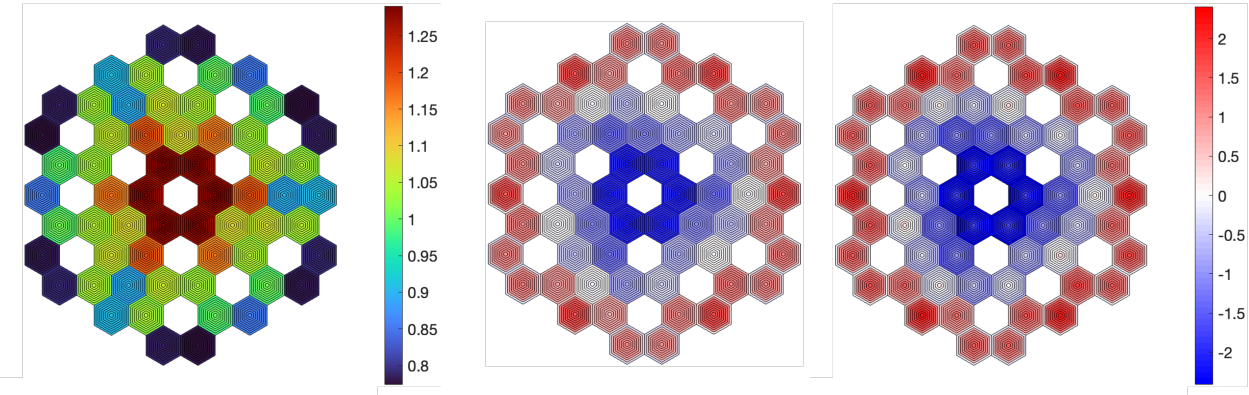

Figure 21: Axially integrated ring-wise fission reaction rates of Serpent (left) and the errors (%) of RH (middle) and SRH (right) vs. Serpent, for the 3D full core.

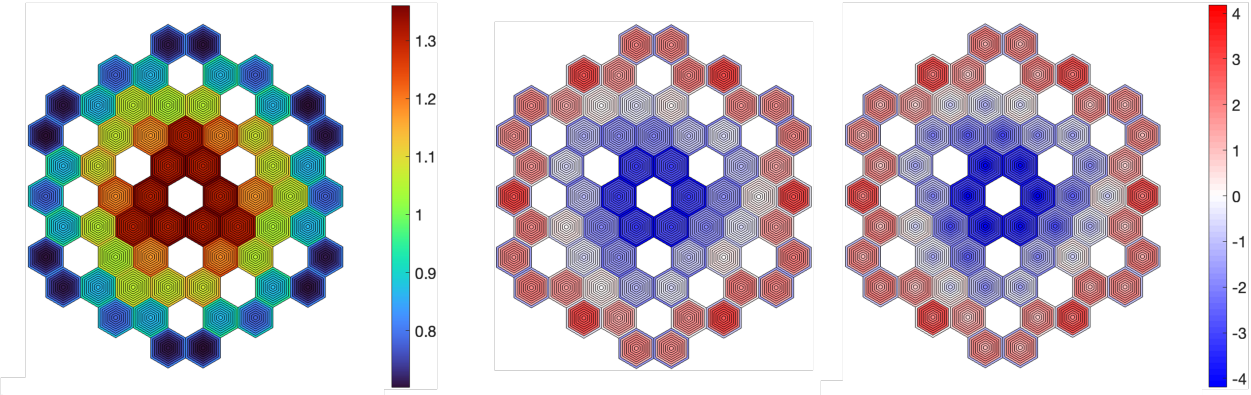

Figure 22: Axially integrated ring-wise absorption reaction rates of Serpent (left) and the errors (%) of RH (middle) and SRH (right) vs. Serpent, for the 3D full core.

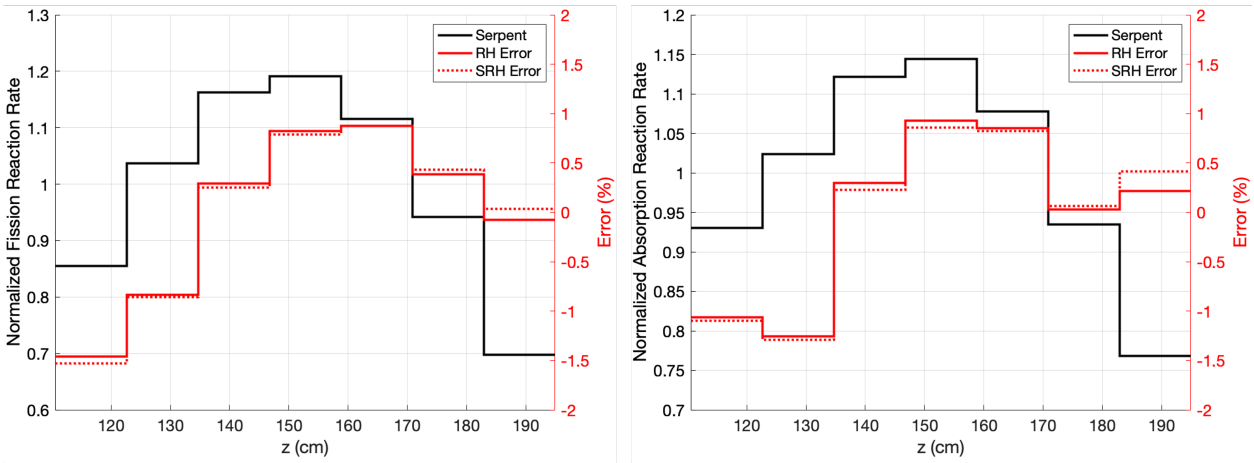

Figure 23: Radially integrated plane-wise fission (left) and absorption (right) reaction rates of Serpent and the errors (%) of RH and SRH vs. Serpent, for the 3D full core.

Table 11: Summary of the 2D and 3D maximum errors and RMSEs (%) of the ring-wise fission and absorption reaction rates for the 3D full core.

Reaction	Error	RH	SRH
Fission	2D Max	2.15	2.40
	2D RMSE	1.01	1.17
	3D Max	3.72	3.96
	3D RMSE	1.31	1.45
Absorption	2D Max	4.04	4.18
	2D RMSE	1.75	1.76
	3D Max	6.10	5.95
	3D RMSE	1.95	1.97

In terms of eigenvalues, RH clearly performs better than SRH: the eigenvalue error of RH vs. Serpent is only 100 pcm, while that of SRH is more than double that value. However, they

present no meaningful differences when comparing reaction rates against Serpent. In terms of fission reaction rates, RH shows slightly better results than SRH: the maximum error and RMSE of RH vs. Serpent are lower than those of SRH by about 0.25% and 0.15%, respectively. In terms of the absorption reaction rates, however, it is hard to claim that one scheme surpasses the other. Their errors in regard to the radially integrated plane-wise reaction rates are also very similar. Nevertheless, SRH reflects the characteristic intra-assembly error shapes, whereas RH presents more-or-less flat error distributions in each assembly. Thus, SRH can still provide reasonably accurate solutions on average, and may be a valid option whenever aggressive memory usage and runtime reduction are required. But RH would generally be more desirable as a result of being more physically consistent with FH.

4.1.5 Full-Core Reactivity Coefficients and Kinetic Parameters

Important reactivity coefficients—namely, the fuel temperature coefficients, radial and axial expansion coefficients, and sodium density coefficients—and kinetics parameters were also compared with Serpent in the context of the 3D full-core problem. The Serpent parameters used here are the same as those used in the 3D full-core case.

The fuel temperature coefficients were calculated by fixing the system temperature at 600 K and changing the fuel temperature from 600 to 900 K, at intervals of 100 K. Although Serpent employs 600 K cross-section libraries for the 700 and 800 K cases (as only cross-section libraries for 600 and 900 K are available), it can perform automatic Doppler broadening of point-wise cross sections to an arbitrary temperature, so the point-wise cross sections are always set to a proper temperature. However, the Doppler broadening cannot be done for unresolved resonance range probability tables, so the bias that stems from using an incorrect temperature for the probability tables should be accounted for. Table 12 quantifies this bias by running the 900 K case with both the 600 and 900 K libraries. When using the 600 K library, the point-wise cross sections will be Doppler-broadened to 900 K, though the probability tables will still remain at 600 K. On the other hand, using the 900 K library will use probability tables and point-wise cross sections at the exact temperature. The table reveals a bias of 16 pcm, and under the assumption that this bias is linear between 600 and 900 K, a correction factor of 0.0533 pcm/K will be applied when computing the fuel temperature coefficients.

Table 12: Bias from the lack of Doppler broadening for unresolved resonance range probability tables.

Fuel Temperature (K)	Library Temperature (K)	Eigenvalue
600	600	1.03444 ($\pm$ 1)
900	600	1.03310 ($\pm$ 1)
900	900	1.03294 ($\pm$ 1)

Table 13 presents the eigenvalues of Serpent, RH, and SRH for different fuel temperatures, along with the corresponding fuel temperature coefficients. The Serpent eigenvalues include the correction factor. RH and SRH are seen to yield identical fuel temperature coefficients that slightly exceed those of Serpent at all temperatures.

Table 13: Comparison of fuel temperature coefficients of Serpent, RH, and SRH.

	Eigenvalue			Reactivity Coefficient (pcm/K)		
Temperature (K)	Serpent	RH	SRH	Serpent	RH	SRH
600	1.03444 ($\pm$ 1)	1.03610	1.03778	-	-	-
700	1.03386 ($\pm$ 1)	1.03543	1.03711	-0.58	-0.67	-0.67
800	1.03336 ($\pm$ 1)	1.03478	1.03645	-0.50	-0.65	-0.66
900	1.03294 ($\pm$ 1)	1.03423	1.03590	-0.42	-0.55	-0.55

The radial expansion coefficients were estimated by adjusting the assembly pitch by 1 mm. This calculation mimics the displacement of assemblies caused by the support plate expansion. The assemblies are assumed to be rigid bodies, meaning that their internal components remain steady, and the sodium region outside the ducts was expanded or contracted accordingly. Table 14 reports the eigenvalues of Serpent, RH, and SRH in light of different assembly pitch changes, along with the corresponding radial expansion coefficients. Although this perturbation involves radial geometry changes, RH and SRH present near-identical radial expansion coefficients, and these exceed the Serpent-generated ones by about 20 pcm/mm.

Table 14: Comparison of radial expansion coefficients of Serpent, RH, and SRH.

	Eigenvalue			Reactivity Coefficient (pcm/mm)		
Pitch Change (mm)	Serpent	RH	SRH	Serpent	RH	SRH
+1	1.02835 ($\pm$ 1)	1.02914	1.03081	-453	-474	-473
0	1.03288 ($\pm$ 1)	1.03388	1.03554	-	-	-
-1	1.03743 ($\pm$ 1)	1.03863	1.04029	-455	-475	-475

To compute the axial expansion coefficients, the fuel height was changed by 40 mm. Furthermore, the number densities of the fuel were changed in accordance with the volumetric changes. As per the height change of the fuel region, the height of the gas plenum region was either increased or decreased, keeping the in-between sodium plenum region constant. This calculation was performed using a no-rod configuration, meaning that the control rods were completely removed from the domain so as to isolate any additional errors that might originate from contact between the fuel and control rods during the expansion. Table 15 summarizes the eigenvalues of Serpent, RH, and SRH in light of different fuel height changes, and gives the corresponding axial expansion coefficients. As expected, RH and SRH yield near-identical axial expansion coefficients, and these are about 2 pcm/mm lower than the Serpent-generated ones, which is considered acceptable.

Table 15: Comparison of axial expansion coefficients of Serpent, RH, and SRH.

	Eigenvalue			Reactivity Coefficient (pcm/mm)		
Height Change (mm)	Serpent	RH	SRH	Serpent	RH	SRH
+40	1.02920 ($\pm$ 1)	1.03103	1.03255	-31.4	-29.7	-29.6
0	1.04174 ($\pm$ 1)	1.04289	1.04439	-	-	-
-40	1.05466 ($\pm$ 1)	1.05503	1.05653	-32.3	-30.4	-30.4

The sodium density coefficients were computed by adjusting the sodium coolant density by 2.5%. Technically, the number densities of sodium included in the smeared lower and upper structures should also have been changed; however, this was ignored for the sake of simplicity. Table 16 presents the eigenvalues of Serpent, RH, and SRH in light of different sodium density changes, along with the corresponding sodium density coefficients. RH yields sodium density coefficients that are slightly closer to Serpent than to SRH, but the coefficients themselves are very small, and the differences not meaningful.

Table 16: Comparison of sodium density coefficients of Serpent, RH, and SRH.

	Eigenvalue			Reactivity Coefficient (pcm/%)		
Na Density Change (%)	Serpent	RH	SRH	Serpent	RH	SRH
+2.5	1.03327 ($\pm$ 1)	1.03428	1.03596	15.6	16.0	16.8
0	1.03288 ($\pm$ 1)	1.03388	1.03554	-	-	-
-2.5	1.03249 ($\pm$ 1)	1.03347	1.03512	15.6	16.4	16.8

Lastly, the adjoint-weighted neutron generation time (Λ) and delayed neutron fraction (β) of Serpent, RH, and SRH are compared in Table 17, where β_i denotes the delayed neutron fraction of the delayed precursor group i. Serpent employed the iterated fission probability method to compute the adjoint-weighted kinetics parameters.

Table 17: Comparison of the kinetics parameters of Serpent, RH, and SRH.

Kinetics Parameter	Serpent	RH	SRH
Λ (s)	3.803E-07 (1.027E-10)	4.162E-07	4.188E-07
β (pcm)	334.65 (0.33)	317.53	317.81
β_1	7.17 (0.05)	8.07	8.07
β_2	64.31 (0.14)	58.02	58.02
β_3	51.63 (0.13)	48.81	48.83
β_4	140.61 (0.21)	113.03	113.16
β_5	57.09 (0.14)	65.82	65.91
β_6	13.83 (0.07)	23.78	23.82

4.2 Coupled Steady State

The multiphysics steady-state solution was run by utilizing 720 processors in INL's Sawtooth high-performance computing cluster. The simulation wall-clock time totalled 96 minutes. Table 18 gives the distribution of time across the various sub-applications. Notably, Griffin and SAM account for the majority of the computational time. Current efforts are underway to optimize the SAM model and the coupling scheme in order to reduce the computational time spent within the thermal-hydraulic solver.

Table 18: Time spent within each of the various sub-applications during the steady-state calculation.

Application	Time Fraction
Griffin	38.96%
SAM	44.92%
BISON (pins)	14.89%
BISON (plate)	1.24%

Fig. 24 illustrates the convergence of various quantities of interest as a function of the number of Picard iterations, including the effective multiplication factor, maximum temperatures of the coolant and fuel, and x-, and z- components of the displacement field. The convergence of all

quantities within a relative tolerance of 10^{-7} indicates that the solution has correctly converged to a fixed point for the multiphysics system of equations. Notably, the effective multiplication factor that converges to a final value of 1.02244 has the highest convergence rate, followed by temperature fields, and then displacements. This observation underscores the significance of displacement in terms of being the most stringent imposable convergence criterion. Another aspect of the multiphysics system convergence is the interplay between the tolerance for the full simulation and the tolerances for the single-physics simulations. In fact, after reaching the 10^{th} Picard iteration, the absolute value of the relative residual increase for both the maximum fuel and coolant temperatures because the relative residual for the multiphysics simulation reaches the tolerance level set in the thermomechanical simulations (i.e., 10^{-8}). However, note that the absolute relative residual continues to decrease as a function of the Picard iteration until it reaches a value of 10^{-7} at the 11^{th} iteration.

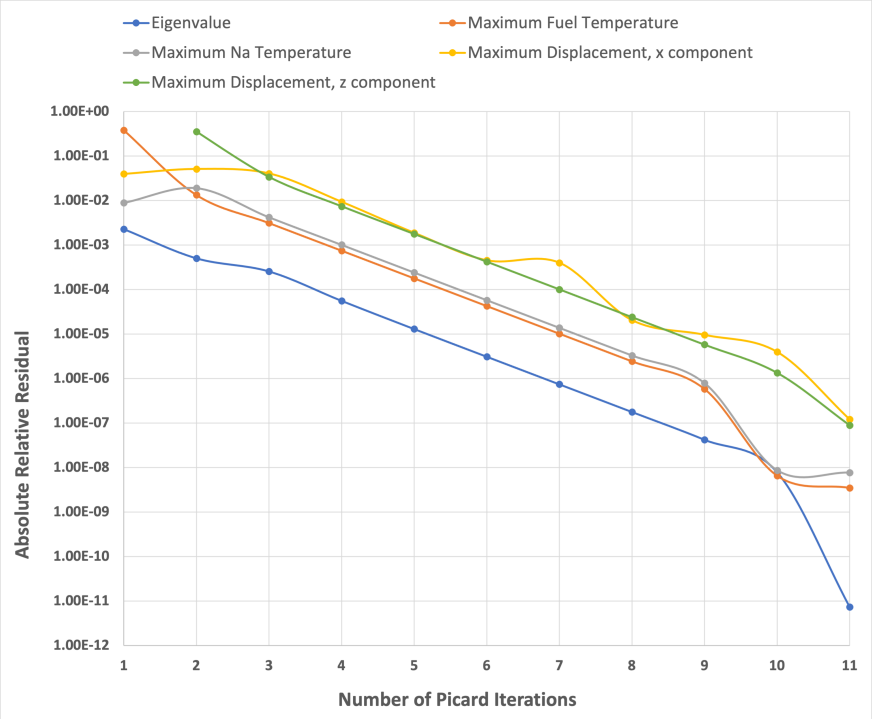

Figure 24: Convergence of quantities of interest as a function of Picard iterations.

Fig. 25.a–c illustrates the steady-state values of the axially integrated power density distribution, fuel temperature, and axial displacement, respectively. Notably, the fuel temperature closely mirrors the power density distribution, as was expected. In this model, in which the fuel axial

displacement is driven solely by thermal expansion, both the fuel temperature and displacement field exhibit similar radial distributions. Although the axial fuel displacement magnitude is on the order of a few centimeters—as is consistent with the literature values of around 4 cm—the maximum axial displacement is less than 1 cm with stress-free temperature of 628 K. This discrepancy arises from the absence of swelling or burnup effects in the BISON model for axial displacement. Future work will investigate inclusion of these phenomena in the full-core ABTR model.

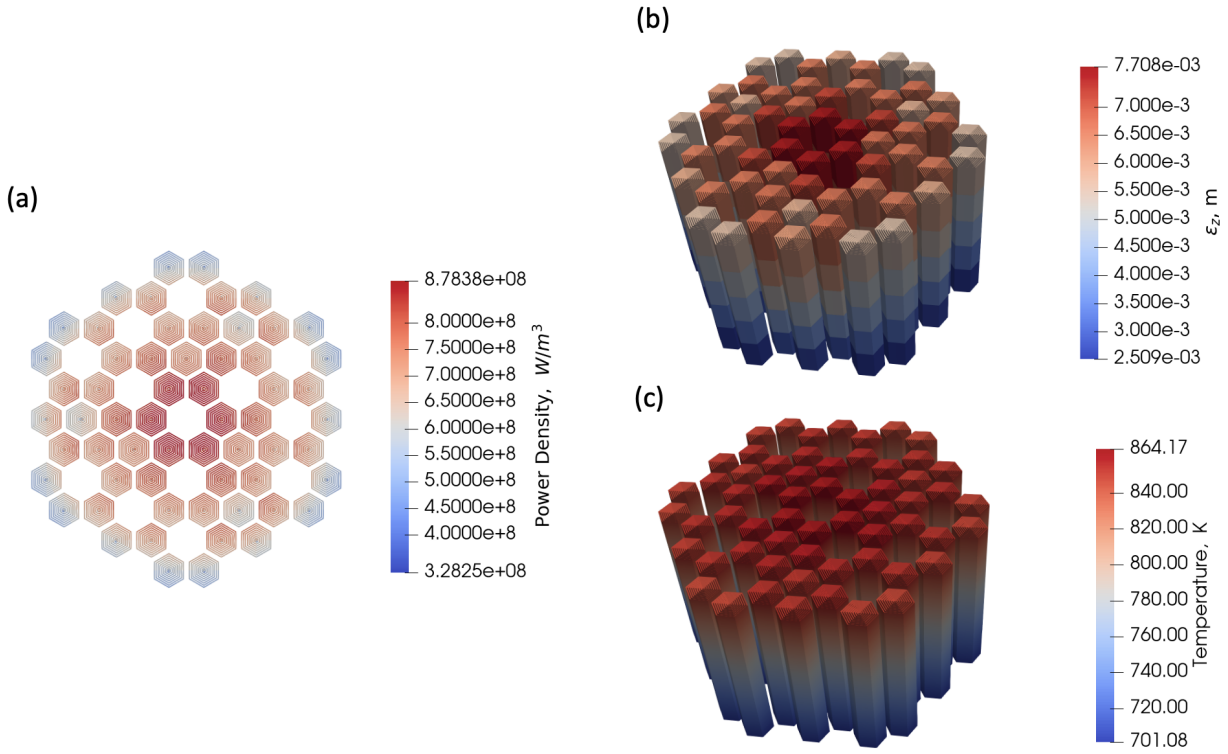

Figure 25: (a) Power density for the fuel mid-plane, (b) 3D fuel temperature distribution, and (c) 3D fuel axial displacement.

Fig. 26.a shows the temperature spatial distribution of the flowing sodium for the fuel assemblies under steady-state condition. Notably, the temperature difference between the inlet and outlet is 146 K, a value consistent with the 150 K reported in Ref. [6]. The density of sodium in fuel assemblies is presented in Fig. 26, showing an inverse proportionality with respect to the temperature profile, with the density decreasing by approximately 5% from inlet to outlet. The temperature of the flowing sodium in the non-fueled assemblies exhibits a near-zero temperature and density change from inlet to outlet, due to the absence of heat deposition in those assemblies and radial assembly-to-assembly heat transfer.

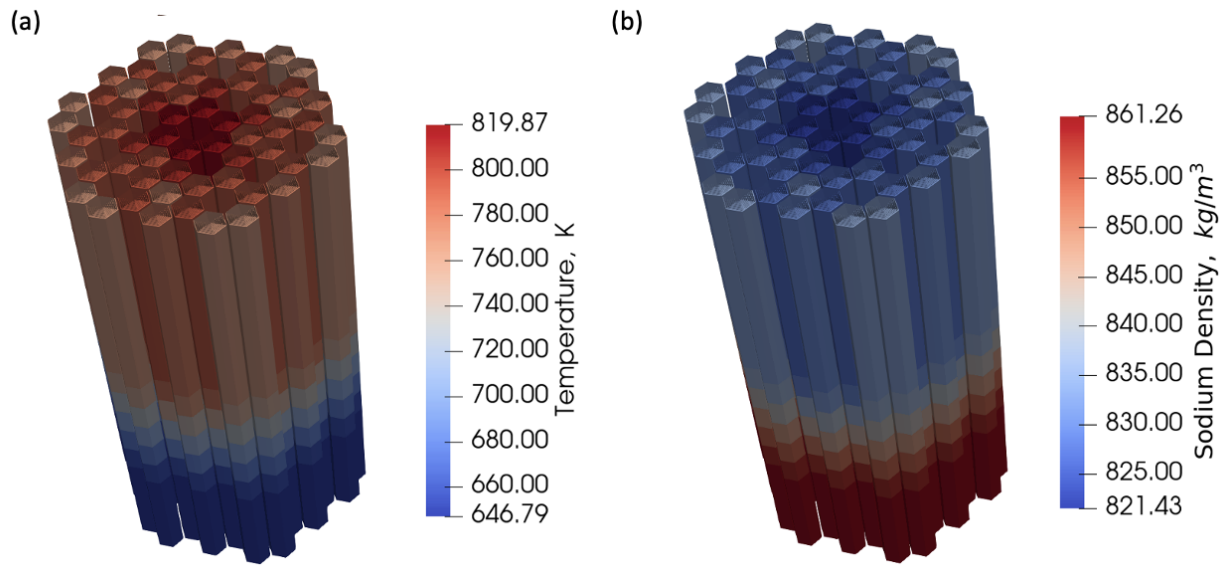

Figure 26: (a) Sodium temperature distribution and (b) sodium density distribution in the fuel channels.

Lastly, Fig. 27 presents the radial displacement field obtained from the support plate model. Under steady-state conditions, the support plate's temperature reaches equilibrium with that of the sodium (i.e., T = 646.3 K throughout). This results in a symmetric solution, with the maximum displacements for the support plate being approximately 1 cm. Hand calculations confirmed that the thermal expansion of the fuel and steel structures fell within the expected bounds for linear expansion at the reference temperature.

4.3 Coupled Transient Results

The ULOF accident scenario was simulated by following the temporal progression outlined in Table 2. As detailed in Section 2.3, the ULOF is a thermal-hydraulics-driven accident scenario in which the pump heads are progressively reduced to zero. The normalized temporal evolution of both the primary and secondary pump's heads is depicted in Fig. 28.a. The pump head value as a function of time for the the primary and secondary pump is retrieved by multiplying the function represented in Fig. 28.a by 415,100 Pa and 40,300 Pa, respectively. These normalization constants were used from the ANL-developed SAM model of the ABTR [27]. It is noticeable that the pump head function does not reach an exact value of zero, but it is set to 0.01% of the initial head after 430 s. This was done to ensure the numerical stability of the numerical multiphysics scheme. Fig. 28.b

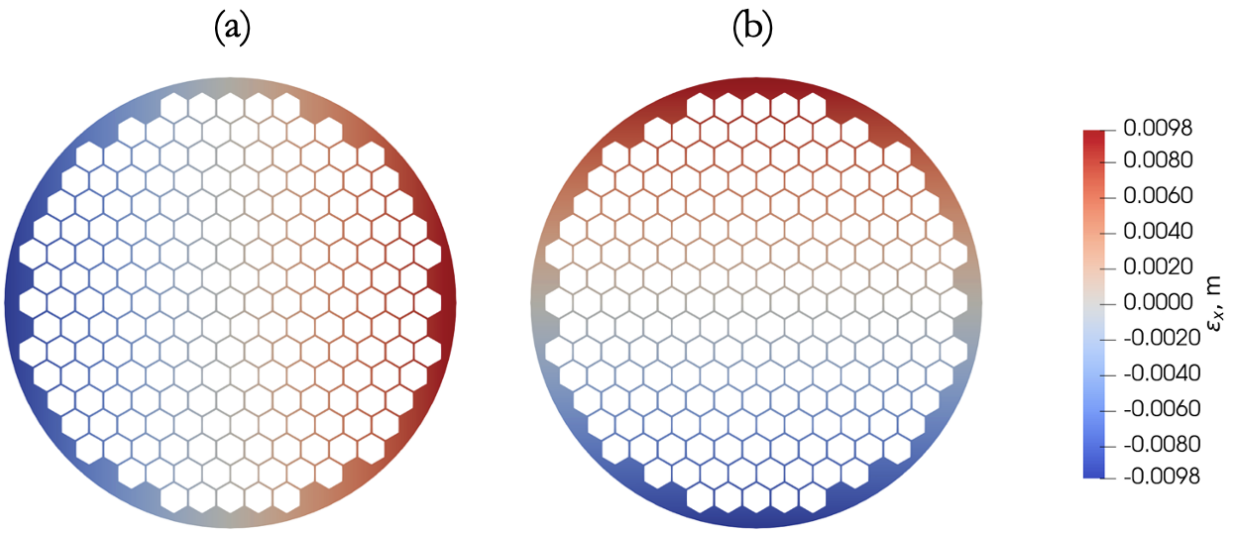

Figure 27: (a) X-component and (b) Y-component of the displacement field for the core's support plate.

illustrates the corresponding reactor power levels, demonstrating a monotonic decrease over time that can be attributed to negative Doppler feedback and axial thermal expansion of the fuel in the first part of the transient, and, then, radial expansion of the support plate. Fig. 28.c reports the power level in one of the ABTR hot channels, located in the first fuel assemblies ring together with the corresponding results from the preliminary safety evaluation report [5]. It is noticeable that the power deposited in the hot channel decreases with time in both cases. However, the power decreases more rapidly for the current simulation and reaches an asymptotic value, dictated by the decay heat that is different than the one reported in Ref. [5]. This discrepancy is mainly caused by two factors: (1) the pump head function used in this work decreases more rapidly than the one used in the preliminary safety evaluation [5], and (2) the decay heat fraction used in this work has a higher value than the one used in Ref. [5], thus leading to a more conservative value of the total power deposited in the hot channel at the end of the transient. This two differences are exacerbated by several differences in the modeling approach, including the use of a spatially-resolved neutronics solution in lieu of a point-kinetic model.

During the initial stages of the transient, the core response is primarily influenced by the fuel temperature and the associated fuel axial displacements—especially when the support plate's contribution is not yet substantial, due to the thermal inertia of the steel structure. Fig. 29 illustrates the midplane fuel temperature for a hot assembly (representative of the innermost ring). Notably,

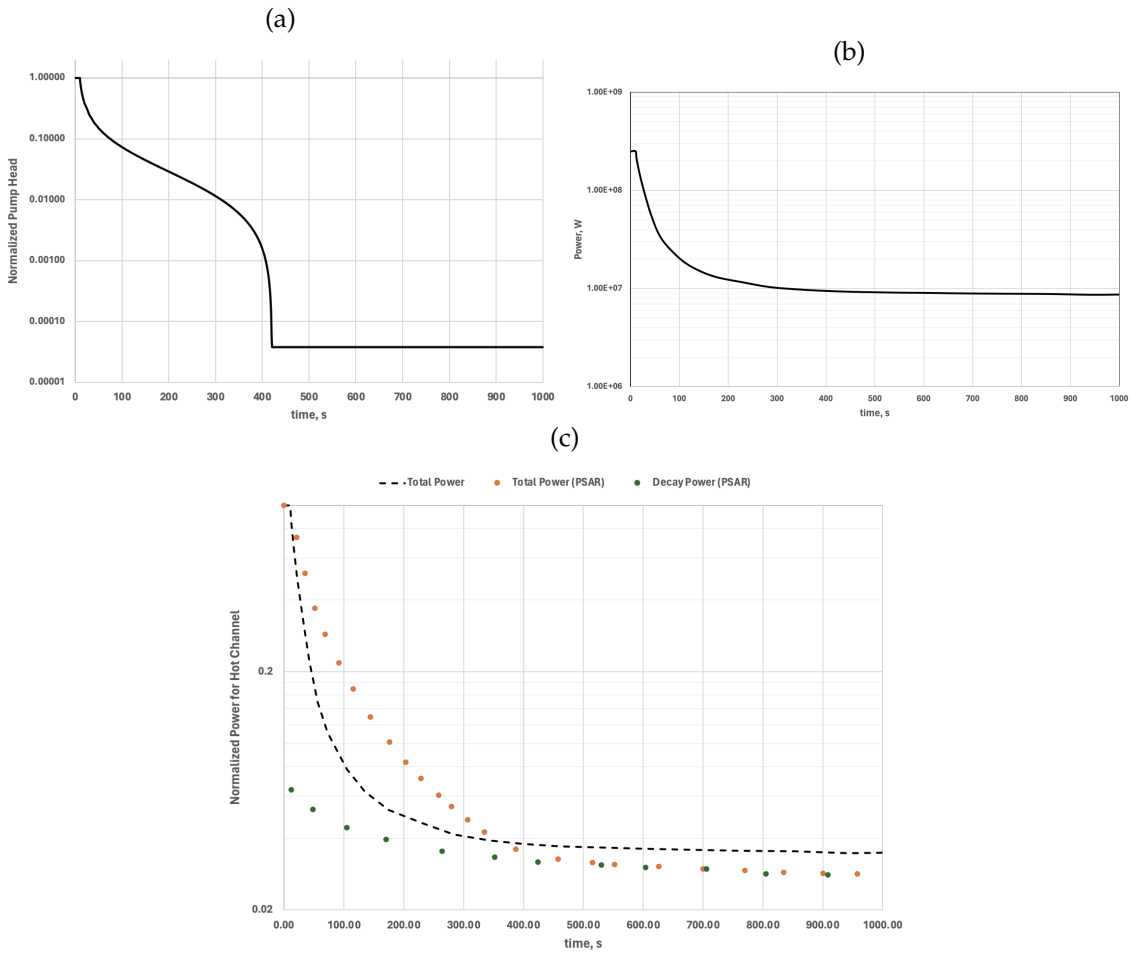

Figure 28: (a) Primary and secondary pump heads as a function of time. Both heads are represented by the same function with different normalization constants. (b) Total power as a function of time (c) Power deposited in the hot channel and comparison against results from Ref. [5].

the temperature initially increases by approximately 30 K within the first 10 seconds of the transient, followed by a subsequent decrease over time due to the negative reactivity feedbacks. This behavior is consistent with the results from the preliminary safety evaluation report, where the fuel temperature peaks at around 923.15 K after the first 10 s in the transient [5]. The corresponding fuel temperature distribution across the core is depicted in the enlarged images above the line plot for the following time steps: 0, 50, 100, and 400 s. Notably, the radial temperature distribution flattens with time due to the sodium mixing during the transient as this mixing leads to a more homogeneous radial temperature profile in the fluid.

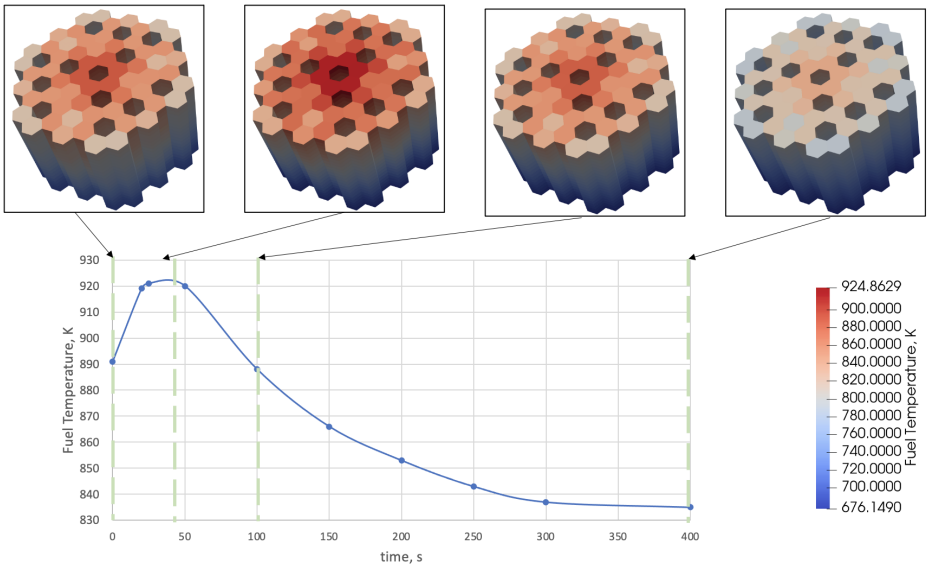

Figure 29: Mid-point fuel temperature for the hot assembly as a function of time, and corresponding full-core radial fuel temperature distribution.

Fig. 30 reports the sodium temperature core-wide distribution for the same time steps as reported for the fuel temperature. Notably, the sodium and fuel temperatures exhibit the same trend during the transient, with the temperature of the fuel exceeding that of the sodium throughout the entire transient, as expected. Comparing the Fig. 30 with the results in Ref. [5], it is noticeable that the peak sodium temperature of 888 K is higher than the value reported in Ref. [5], where the peak is at 873 K. Further investigations will be performed to understand the reason of this discrepancy.

The negative reactivity effect intensifies as the support plate expands, leading to increased inter-assembly distances and the creation of neutron streaming paths. Displacements for the support plate, as well as the temperatures of the cold and hot pools, are presented in Fig. 31.a–b. Notably, the support plate displacement follows the trend of the cold pool, remaining below 1 mm (more specifically, around 0.9 mm). This corresponds to approximately 0.1mm of displacement of each assembly, and considering the reactivity coefficient of 473 pcm/mm, it will result in an insertion worth of approximately -0.15 \$ negative reactivity during the transient. Furthermore, the negative reactivity feedback from the support plate does not manifest instantaneously, as observed in the fuel temperature (discussed in the subsequent figure) or axial displacement, due to the thermal inertia of the support plate. The cold pool temperature that drives the support plate expansion gradually increases due to mixing with the upper plenum sodium. Notably, it is

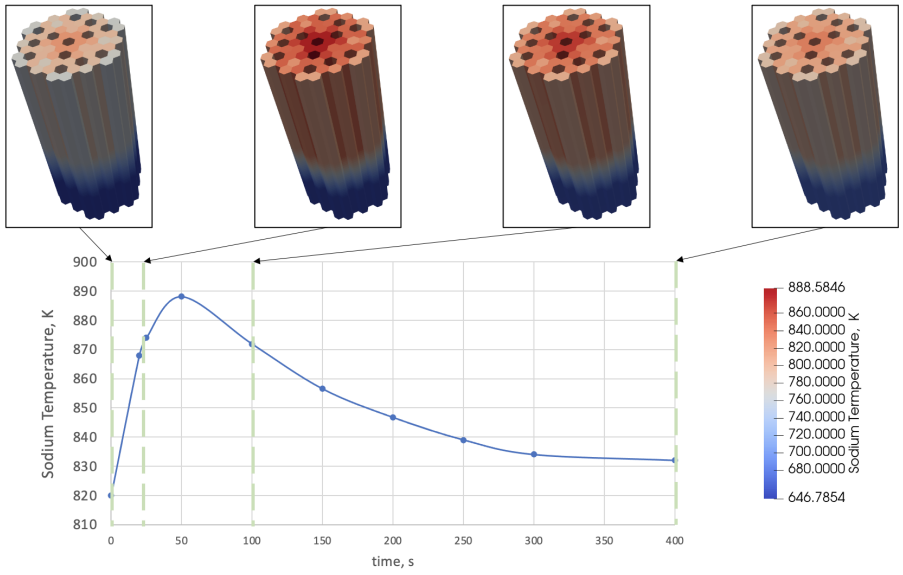

Figure 30: Maximum sodium temperature for the hot assembly upper plane as a function of time, and the corresponding sodium temperature spatial distribution in the fuel channels.

expected that the entire amount of sodium will eventually tend to an equilibrium state characterized isothermal temperature of approximately 830 K, which is the asymptotic value reached in the hot pool. This is because, in the ABTR design, as for any pool-type SFR design, the hot and cold pools are connected.

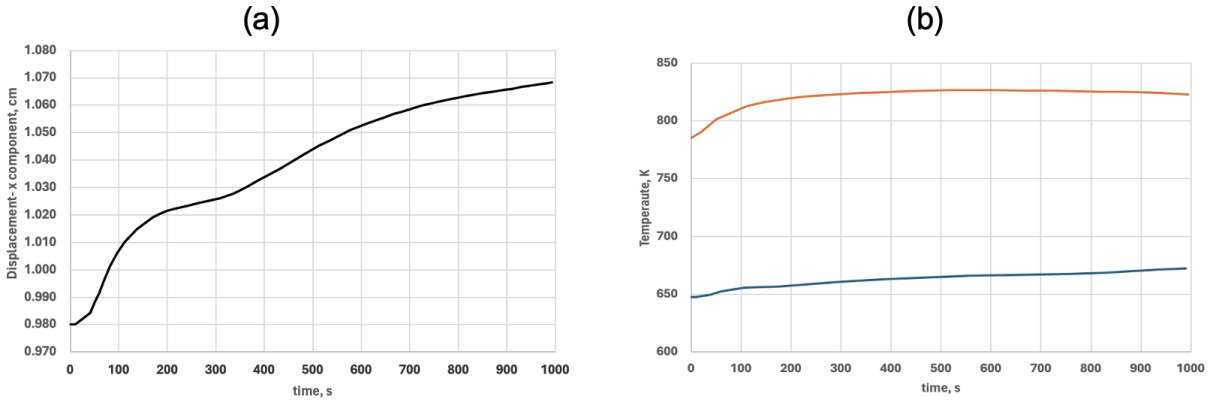

Figure 31: (a) x-component of the support plate displacement. (b) Cold and hot pool temperature as a function of time.

5. CONCLUSIONS AND FUTURE WORK

This report details the progress and activities of INL in regard to the U.S. Nuclear Regulatory Commission project "Development and Modeling Support for Advanced Non-Light Water Reactors"—specifically, with the sodium fast reactor reference plant model.

Several improvements were made to the reference plant model developed in Task 4b. (1) The discrete ordinates method was used in lieu of the super-homogenization (SPH)-corrected diffusion approximation in order to better capture the anisotropic scattering contribution and the change in neutron leakage due to thermal expansion. (2) The novel neutronic spatial discretization approach, termed the RH approximation, was introduced to capture the differential expansion of the materials in the core. The new technique proved successful at preserving fission rates and keeping the eigenvalue within 2.5% and 266 pcm, respectively. Separation of the different materials in the core enables the differential expansion of materials to be explicitly accounted for, eliminating the need for problem-specific cross-section functionalization techniques. (3) The SAM model for the core and system thermal-hydraulics analysis was updated to include 61 channels instead of just four representative channels. This allows users to obtain improved spatial resolution for sodium temperature and density. (4) All the meshes were created via the MOOSE Reactor module, eliminating the reliance on external tools for mesh creation. (5) The fuel axial expansion now leverages the HT9 and UPuZr material properties that have been validated against experimental data for metallic fuel". (6) Finally, the support plate thermomechanical model was updated to capture the thermal inertia of the steel, thus leading to more conservative transient results. The reference plant model was used to perform full-core ULOF transient calculations, including neutronics, thermal, and mechanical feedback mechanisms.

Future work may be devoted to further improving the ABTR model to:

1. Incorporate the new Griffin workflow for mesh preparation and cross section preparation
2. Verify the control rod worth calculated in Griffin versus the Serpent model
3. Include the control rod-drive line expansion reactivity feedback mechanism that is currently not captured.
4. Use the model to simulate a reactivity insertion accident scenario.

5. Further improve the support plate expansion model to include realistic design specifications and capture the 3D thermomechanics more accurately. With resistance to the pad.

6. Include inter-assembly heat transfer after assessment of its relative importance with respect to other heat transfer mechanisms.

7. Remove intermediate model unless inter-assembly heat transfer is important

8. investigate the deployment of the Pronghorn sub-channel model to obtain better thermal fluids resolution. This would entail the reconstruction of the pin powers from the RH neutronics mesh. Channel block

9. Model non-local heat deposition, comprehending gamma heating, during steady state and transient conditions. This involves addition flow channels to model cooling of peripheral assemblies.

10. Further improve the plena mixing model to account for realistic sodium stratification.

11. Further investigate the discrepancies between the current analysis and previous results in literature.

REFERENCES

[1] T. K. Kim, "Benchmark specification of advanced burner test reactor," Tech. Rep. ANL/NSE-20/65, Argonne National Laboratory, 2020.

[2] C. M. Mueller, C.-S. Lin, and J. Ortensi, "Nrc multiphysics analysis capability deployment (fy2021 - part 2)," Tech. Rep. INL/EXT-21-62522-Rev000, Idaho National Laboratory, 4 2021.

[3] E. Shemon, Y. Yu, H. Park, and C. Brennan, "Assessment of Fast Reactor Hot Channel Factor Calculation Capability in Griffin and NekRS," Tech. Rep. ANL/NSE-21/42, Argonne National Laboratory, Lemont, IL, 2021.

[4] E. R. Shemon, J. J. Grudzinski, C. H. Lee, J. W. Thomas, and Y. Q. Yu, "Specification of the advanced burner test reactor multi-physics coupling demonstration problem," Tech. Rep. ANL/NE-15/43, Argonne National Laboratory, 12 2015.

[5] F. E. Dunn, T. H. Fanning, and J. E. Cahalan, "Preliminary safety evaluation of the advanced burner test reactor.," Tech. Rep. ANL-AFCI-172, Argonne National Laboratory, 9 2006.

[6] T. K. Kim, "Benchmark specification of advanced burner test reactor," Tech. Rep. ANL/NSE-20/65, Argonne National Laboratory, December 2020.

[7] N. Choi, S. Terlizzi, Y. Wang, H. Park, C. Lee, and J. Ortensi, "Investigation of ring-heterogeneous geometry approximation for efficient and practical sfr analysis," in *International Conference on Physics of Reactors (PHYSOR 2024)*, pp. 1213–1216, April 2024.

[8] Hummel and Okrent, *Reactivity Coefficients in Large Fast Power Reactors*. American Nuclear Society, 1970.

[9] R. N. Hill, "Fast reactor physics –2 reactivity feedbacks and fuel cycle," Presented at the NRC Fast Reactor Technology Training Curriculum, March 2019.

[10] K.-i. Kawada, I. Sato, Y. Tobita, W. Pfrang, L. Buffe, and E. Dufour, "Development of pirt (phenomena identification and ranking table) for sas-sfr (sas4a) validation," in *Proceedings of the 2014 22nd International Conference on Nuclear Engineering ICONE22*, 2014.

[11] Y. Chang, P. Finck, and C. Grandy, "Advanced burner test reactor preconceptual design report," Tech. Rep. ANL-AFCI-173, Argonne National Laboratory, 2006.

[12] D. R. Gaston, C. J. Permann, J. W. Peterson, A. E. Slaughter, D. Andrš, Y. Wang, M. P. Short, D. M. Perez, M. R. Tonks, J. Ortensi, L. Zou, and R. C. Martineau, "Physics-based multiscale coupling for full core nuclear reactor simulation," *Annals of Nuclear Energy*, vol. 84, pp. 45–54, 2015.

[13] C. Lee, Y. S. Jung, H. Park, E. R. Shemon, J. Ortensi, Y. Wang, V. M. Laboure, and Z. M. Prince, "Griffin software development plan," Tech. Rep. INL/EXT-21-63185, Idaho National Laboratory, 6 2021.

[14] R.L. Williamson et al., "Multidimensional Multi-physics Simulation of Nuclear Fuel Behavior," *Jou. Nucl. Mat.*, vol. 423, no. 149–163, 2012.

[15] R. Hu, L. Zou, G. Hu, D. Nunez, T. Mui, and T. Fei, "Sam theory manual," Tech. Rep. ANL/NSE-17/4, Argonne National Laboratory, 2017.

[16] E. Shemon, Y. Miao, S. Kumar, K. Mo, Y. S. Jung, A. Oaks, S. Richards, G. Giudicelli, L. Harbour, and R. Stogner, "Moose reactor module: An open-source capability for meshing nuclear reactor geometries," *Nuclear Science and Engineering*, vol. 0, no. 0, pp. 1–25, 2023.

[17] S. Terlizzi and V. Labouré, "Asymptotic hydrogen redistribution analysis in yttrium-hydride-moderated heat-pipe-cooled microreactors using direwolf," *Annals of Nuclear Energy*, vol. 186, p. 109735, 2023.

[18] M. K. Mohammad Jaradat and J. Ortensi, "Thermal spectrum molten salt-fueled reactor reference plant model," Tech. Rep. INL/RPT-23-72875-Rev000, Idaho National Laboratory, July 2023.

[19] Z. M. Prince, P. Balestra, J. Ortensi, S. Schunert, O. W. Calvin, J. Hanophy, K. Mo, and G. Strydom, "Sensitivity analysis, surrogate modeling, and optimization of pebble-bed reactors considering normal and accident conditions," 2024.

[20] C.-S. Lin and W. S. Yang, "An assessment of the applicability of multigroup cross sections generated with monte carlo method for fast reactor analysis," *Nuclear Engineering and Technology*, vol. 52, no. 12, pp. 2733–2742, 2020.

[21] Z. M. Prince, J. T. Hanophy, V. M. Labouré, Y. Wang, L. H. Harbour, and N. Choi, "Neutron transport methods for multiphysics heterogeneous reactor core simulation in griffin," *Annals of Nuclear Energy*, vol. 200, p. 110365, 2024.

[22] W. C. Dawn, J. Ortensi, M. D. DeHart, and S. P. Palmtag, "Comparison of generation of higher-order neutron scattering cross sections," tech. rep., Idaho National Laboratory, 1 2020.

[23] C. Lee, Y. S. Jung, and W. S. Yang, "MC2-3: Multigroup Cross Section Generation Code for Fast Reactor Analysis," Tech. Rep. ANL/NE-11/41 Rev.3, Argonne National Laboratory, August 2018.

[24] R. E. Alcouffe, F. W. Brinkley, D. R. Marr, and R. D. O'Dell, "User's guide for twodant: a code package for two-dimensional, diffusion-accelerated, neutral-particle transport," tech. rep., Los Alamos National Laboratory, 3 1984.

[25] J. Hader, E. Shemon, and C. Lee, "Initial verification of heterogeneous multigroup cross sections in mc23/proteus," in *Transactions of the American Nuclear Society*, pp. 1213–1216, 2014.

[26] G. Hu, G. Zhang, and H. R., "Reactivity feedback modeling in sam," Tech. Rep. ANL-NSE19, Argonne National Laboratory, December 2019.

[27] G. Hu, G. Zhang, and R. Hu, "Reactivity Feedback Modeling in SAM.," tech. rep., 2019.